INTERNATIONAL JOURNAL FOR NUMERICAL METHODS IN ENGINEERING
Int. J. Numer. Meth. Engng 2015; **102**:1211–1237
Published online 5 August 2014 in Wiley Online Library (wileyonlinelibrary.com). DOI: 10.1002/nme.4743

Model order reduction for meshfree solution of Poisson singularity problems

Jiun-Shyan Chen[1,*,†], Camille Marodon[2] and Hsin-Yun Hu[3]

[1]*Structural Engineering Department, University of California, San Diego (UCSD), La Jolla, CA 92093-0085, USA*
[2]*Civil and Environmental Engineering Department, University of California, Los Angeles (UCLA), Los Angeles, CA 90095-1593, USA*
[3]*Applied Mathematics Department, Tunghai University, Taichung 407, Taiwan*

SUMMARY

Model order reduction (MOR) techniques for enriched reproducing kernel meshfree methods are proposed for analysis of Poisson problems with mild and strong singularities. The employment of an integrated singular basis function method (ISBFM), in conjunction with the selection of harmonic near-tip asymptotic basis functions, leads to a Galerkin formulation in which the non-smooth near-tip basis functions appear only on the boundaries away from the singularity point. This approach avoids the need of integrating the derivatives of non-smooth functions near the singularity point and yields a discrete system that allows effective MOR procedures. Under this framework, a decomposed reduction method equipped with two distinct projections for smooth and non-smooth parts of the finite-dimensional space is proposed. Compared with the uniform reduction approach using a single projection operator, the decomposed projection on ISBFM discrete system preserves the singularity behavior of the fine-scale solution in its lower-dimensional approximation. Analytical error estimation and stability analysis show that ISBFM with the decomposed projection can achieve better accuracy with only a slight increase of condition number compared with the uniform reduction approach in the reduced-order solution of singularity problems. The numerical tests validate the effectiveness of the proposed methods. Copyright © 2014 John Wiley & Sons, Ltd.

Received 3 March 2014; Revised 9 June 2014; Accepted 17 June 2014

KEY WORDS: model order reduction; reproducing kernel approximation; meshfree methods; decomposed projection; singularity problems

1. INTRODUCTION

Model order reduction (MOR) methods have been shown to be effective in solving large-scale systems [1]. A great number of MOR analyses are based on the SVD [2] and rely on eigenvector analysis to provide an approximation of the original system. The POD method [3], introduced by Kosambi [4], determines a lower-dimension approximation of a discrete system by constructing a projection onto a space spanned by the dominant SVD modes. The POD method was proven to be the optimal lower-dimension approximation in the mean squared error [5]. Everson and Sirovich [6] proposed the snapshot POD method that constructs the subspace of the reduced model based on data collected by snapshots or samples of the solution. The SVD MOR techniques have been applied to turbulence [7], fluid mechanics [8–10], micro-electromechanical systems [11], and parameterized static problems [12], among others. However, the method of snapshots is not completely thorough and requires further investigation. The moment-matching methods, such as the Krylov subspace method [13, 14], provide a reduced model based on an approximation of the transfer function of the discrete system in the frequency domain, by the mean of Laplace transform.

*Correspondence to: Jiun-Shyan Chen, Structural Engineering Department, University of California, San Diego (UCSD), La Jolla, CA 92093-0085, USA.
†E-mail: js-chen@ucsd.edu

While MOR methods have been proposed for various fields in science and engineering, its application to problems with singularities is juvenile. For such problems, the MOR methods need to consider the lack of regularity in the numerical solution's finite-dimensional space. Numerical methods with smooth approximation and polynomial reproducibility, such as reproducing kernel (RK) particle method [15, 16], often rely on adaptive refinements in the vicinity of the singularity to achieve accuracy [17] or enrichment of smooth approximation. The latter is carried out by embedding the near-tip characteristics in the smooth approximation [18–20] under the framework of extended finite-element methods [21–23] or enriched meshfree methods [24–26]. The asymptotic solutions near the singularity point have been derived explicitly for Poisson problems with mild and strong singularities [19, 27] and have also been successfully used in the enriched approximation space [23, 26, 28].

While enriching the approximation with proper singularity characteristics in the basis functions enhances approximation accuracy, the ability to integrate those non-smooth basis functions to a desired order of accuracy effectively for the Galerkin procedure is not straightforward. The integrated singular basis function method (ISBFM) [28] has been introduced to address this issue. In ISBFM, the selected near-tip basis functions satisfy the homogeneous differential equation with particular conditions on the boundaries adjacent to the singularity point, and the Galerkin equation is formulated such that the near-tip basis functions do not appear in integrals near the singularity point. As such, quadrature issues in the domain integral and boundary integrals near the singularity point are relieved.

In this work, we consider reduced-order modeling of Poisson problems with mild and strong singularities using enriched RK approximation under the ISBFM Galerkin framework. The employed near-tip basis functions are global harmonic functions that are homogeneous on the Dirichlet boundary and derivative homogeneous on the Neumann boundary, adjacent to the singularity point. With additional integration by parts in the Galerkin procedure, the near-tip basis functions appear only on the boundaries away from the singularity point in the resulting Galerkin equation. Consequently, the domain integration of the near-tip basis function derivatives near the singularity point is avoided, and the corresponding discrete system can be partitioned for independent projections of DOFs associated with smooth and non-smooth approximation functions. With such a discrete system, we introduce in this paper a block diagonal projection matrix composed of two distinct reduced projections to the smooth and non-smooth parts of the approximation and considering that the number of non-smooth basis functions is much smaller than the dimension of the smooth part of the approximation.

Block-preserving MOR methods have been proposed in the field of coupled and interconnected systems [29–31] to preserve the interconnection relations between subsystems or physical subdomains in the context of linear time-invariant systems. The projection matrix in the block-preserving MOR is constructed from the matrices associated with each subsystem. In this work, the submatrices associated with the smooth and non-smooth basis functions are not fully decoupled because of the overlapping supports between the smooth and non-smooth basis functions. As such, our proposed decomposed projection matrix for singularity problems is constructed based on the Schur complement of the original system, rather than using the sub-matrix associated with the smooth basis functions. This approach enables significant dimension reduction of the smooth approximation while capturing the singularity behavior. The analytical estimation of the reduced solution error and the stability of the reduced system in the form of condition numbers, as well as operation count of the two reduced-order projection methods, are also provided in this work.

The outline of this paper is as follows. Characteristics and approximation methods for Poisson problems with singularities are first introduced in Section 2. An overview of the ISBFM along with enriched RK approximation is given in Section 3. In Section 4, two proposed MOR methods for Poisson singularity problems that are well suited to the resulting discrete system are introduced. The strategy of decomposed projection is presented in this section as well. In Section 5, the error estimation for the two MOR methods is given, and the stability of the reduced systems is analyzed by the estimated condition numbers of the reduced discrete systems. Section 6 presents numerical experiments to demonstrate the effectiveness of the proposed methods and the reliability of the error and stability estimations. Finally, conclusions and remarks are given in Section 7.

DOI: 10.1002/nme

2. PRELIMINARIES

The characteristics of the singularity problems and the associated numerical solution techniques are first reviewed in this section to allow effective construction of reduced-order formulation.

2.1. Model problem

We consider problems with singularities induced by the following: (i) the roughness in the non-convex boundary geometry and (ii) the discontinuities in the boundary conditions. For demonstration purpose, consider the following boundary value problem:

$$\begin{aligned} \Delta u + s &= 0 \quad \text{in} \quad \Omega \\ u &= g \quad \text{on} \quad \Gamma_g \\ \nabla u \cdot \boldsymbol{n} &= h \quad \text{on} \quad \Gamma_h \end{aligned} \tag{1}$$

where $\Delta = \nabla \cdot \nabla$, Ω is a bounded domain with concave boundary $\partial\Omega = \Gamma = \Gamma_g \cup \Gamma_h$, the vector $\boldsymbol{n}$ is the outward normal of $\partial\Omega$, and s, g, and h are smooth functions.

In Figure 1, there is a singularity in the derivative of the solution at point S when $\Theta > \pi$. The order of singularity is affected by the angle Θ as well as the type of boundary conditions on the two boundaries Γ_{s1} and Γ_{s2} connected to the point S, and we denote $\Gamma_s = \Gamma_{s1} \cup \Gamma_{s2}$. Two combinations of boundary conditions on Γ_{s1} and Γ_{s2} are considered: pure Dirichlet (D–D) or mixed Neumann and Dirichlet (N–D) boundary conditions. The basis functions of the harmonic asymptotic solution [27] of the problem in (1) near the singularity point have been used as the enrichment functions in the numerical solution of singularity problems. The forms of the solution near the singularity point for different singularity problems, presented in Figure 2, are summarized in Table I [32–34], wherein r is the distance between any point in the domain and the singularity point.

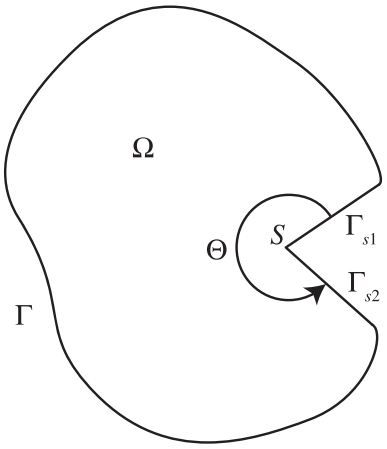

Figure 1. Model of general singularity problem.

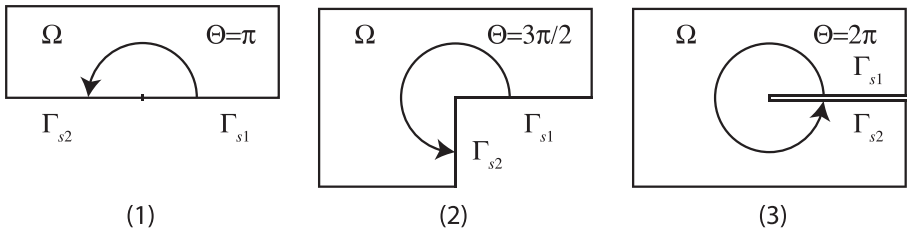

Figure 2. Different types of geometric singularities.

DOI: 10.1002/nme

Table I. Order of singularity for harmonic solutions of problems with D–D or N–D types of boundary conditions.

	$\Theta = \pi$	$\Theta = \frac{3\pi}{2}$	$\Theta = 2\pi$
D–D type	$O(r)$	$O\left(r^{\frac{2}{3}}\right)$	$O\left(r^{\frac{1}{2}}\right)$
N–D type	$O\left(r^{\frac{1}{2}}\right)$	$O\left(r^{\frac{1}{3}}\right)$	$O\left(r^{\frac{1}{4}}\right)$

Table II. Non-smooth basis functions F_m.

	F_m	α_m
D–D type	$r^{\alpha_m}\sin(\alpha_m\theta)$	$\frac{(m-1)\pi}{\Theta}$
N–D type	$r^{\alpha_m}\cos(\alpha_m\theta)$	$\frac{(m-1/2)\pi}{\Theta}$

2.2. *Near-tip asymptotic expansion*

Different treatments of the numerical approximation, such as adaptive refinement near the singularity point or embedding singularity behavior in the approximation space by the means of enrichments [19–22], have been investigated to improve the accuracy of the approximated solution, and the latter is introduced in this study. The asymptotic expansion of the solution near the singularity can be expressed as follows

$$u(\boldsymbol{x}) = \sum_{m=1}^{\infty} a_m F_m(\boldsymbol{x}), \quad \text{as } \boldsymbol{x} \to \mathbf{x}_S \tag{2}$$

where F_m are asymptotic basis functions as shown in Table II [27] for the corresponding singularity problems presented in Table I and $\boldsymbol{x}_S$ is the coordinate of the singularity point. Each non-smooth basis function F_m satisfies the following conditions:

$$\begin{cases} \Delta F_m = 0 & \text{in} \quad \Omega \\ F_m = 0 & \text{on} \quad \Gamma_g \cap \Gamma_s \\ \nabla F_m \cdot \boldsymbol{n} = 0 & \text{on} \quad \Gamma_h \cap \Gamma_s \end{cases} \tag{3}$$

Although in (3) the near-tip bases yield homogeneous boundary conditions, their employment in approximating general nonhomogeneous boundary conditions in the model problem in (1) can be achieved by adding the particular solution in the approximation as have been discussed in [27]. Further, these near-tip asymptotic basis functions are global functions, and this needs to be considered in the imposition of boundary conditions away from the singularity point. It is also worth noting that when these near-tip basis functions are used in the approximation, high-order quadrature rules are needed near the singularity point. The ISBFM Galerkin formulation [35–37] can be employed to avoid taking the integration of the near-tip basis functions in the domain and on boundaries near the singularity point. The detailed formulation of this ISBFM Galerkin formulation is given in the next section.

3. ISBFM GALERKIN APPROXIMATION

In this section, the ISBFM Galerkin formulation in conjunction with Nitsche's method for singularity problems will be introduced. These basic formulations constitute the framework for the construction of the full model for the proposed reduced-order methods.

DOI: 10.1002/nme

3.1. ISBFM Galerkin formulation

The functional associated with the model problem in (1) is

$$I = \frac{1}{2}\int_{\Omega} \nabla u \cdot \nabla u \mathrm{d}\Omega - \int_{\Gamma_h} uh \mathrm{d}\Gamma \tag{4}$$

where $u \in \mathrm{H}_g^{1+\alpha}(\Omega)$ with α is the order of asymptotic behavior near the singularity point described in Table I and considering no source term for clarity. Let the approximation of u, denoted as u^h, be decomposed into a smooth part $\bar{u}^h$ and a non-smooth part $\hat{u}^h$ as

$$u^h = \bar{u}^h + \hat{u}^h \tag{5}$$

Here, an RK approximation is introduced for the smooth solution, while the near-tip asymptotic functions given in Section 2.2 are employed for the non-smooth part of the solution, and these will be discussed in Section 3.2. For simplicity, we consider in the following that the Dirichlet and Neumann boundary conditions are homogeneous on the adjacent boundaries associated with the singularity point S; that is, $g = 0$ on $\Gamma_g \cap \Gamma_s$, and $h = 0$ on $\Gamma_h \cap \Gamma_s$. The case of nonhomogeneous boundary conditions is discussed in Section 2.2 and referred to [27].

The functional (4) is discretized and modified for imposition of the essential boundary conditions on Γ_g using Nitsche's method [38, 39] as

$$\begin{aligned} I = &\frac{1}{2}\int_{\Omega} \nabla\left(\bar{u}^h + \hat{u}^h\right) \cdot \nabla\left(\bar{u}^h + \hat{u}^h\right) \mathrm{d}\Omega - \int_{\Gamma_h} \left(\bar{u}^h + \hat{u}^h\right) h \mathrm{d}\Gamma \\ &- \int_{\Gamma_g} \nabla\left(\bar{u}^h + \hat{u}^h\right) \cdot \boldsymbol{n} \left(\bar{u}^h + \hat{u}^h - g\right) \mathrm{d}\Gamma + \frac{\beta}{2}\int_{\Gamma_g} \left(\bar{u}^h + \hat{u}^h - g\right)\left(\bar{u}^h + \hat{u}^h - g\right) \mathrm{d}\Gamma \end{aligned} \tag{6}$$

Two boundary integrals on Γ_g are due to Nitsche's enforcement of essential boundary conditions, and β is a penalty parameter. Minimizing the functional in (6) leads to the following two Galerkin equations:

$$\begin{aligned} &\int_{\Omega} \nabla \delta\bar{u}^h \cdot \nabla\left(\bar{u}^h + \hat{u}^h\right) \mathrm{d}\Omega \\ &- \int_{\Gamma_g} \left(\delta\bar{u}^h \left(\nabla\left(\bar{u}^h + \hat{u}^h\right) \cdot \boldsymbol{n} - \beta\left(\bar{u}^h + \hat{u}^h\right)\right) + \nabla\delta\bar{u}^h \cdot \boldsymbol{n}\left(\bar{u}^h + \hat{u}^h\right)\right) \mathrm{d}\Gamma \\ = &\int_{\Gamma_h} \delta\bar{u}^h h \mathrm{d}\Gamma - \int_{\Gamma_g} \left(-\delta\bar{u}^h \beta g + \nabla\delta\bar{u}^h \cdot \boldsymbol{n} g\right) \mathrm{d}\Gamma \end{aligned} \tag{7a}$$

$$\begin{aligned} &\int_{\Omega} \nabla \delta\hat{u}^h \cdot \nabla\left(\bar{u}^h + \hat{u}^h\right) \mathrm{d}\Omega \\ &- \int_{\Gamma_g} \left(\delta\hat{u}^h \left(\nabla\left(\bar{u}^h + \hat{u}^h\right) \cdot \boldsymbol{n} - \beta\left(\bar{u}^h + \hat{u}^h\right)\right) + \nabla\delta\hat{u}^h \cdot \boldsymbol{n}\left(\bar{u}^h + \hat{u}^h\right)\right) \mathrm{d}\Gamma \\ = &\int_{\Gamma_h} \delta\hat{u}^h h \mathrm{d}\Gamma - \int_{\Gamma_g} \left(-\delta\hat{u}^h \beta g + \nabla\delta\hat{u}^h \cdot \boldsymbol{n} g\right) \mathrm{d}\Gamma \end{aligned} \tag{7b}$$

which are referred to as the standard Galerkin formulation. If the basis functions for the non-smooth part of the solution $\hat{u}^h$ are harmonic, that is, $\Delta\hat{u}^h = 0$, the domain integral involving $\hat{u}^h$ can be expressed as a boundary integral by applying integration by parts to yield

$$\int_{\Omega} \nabla v \cdot \nabla\hat{u}^h \mathrm{d}\Omega = \int_{\Gamma} v \nabla\hat{u}^h \cdot \boldsymbol{n} \mathrm{d}\Gamma, \ \forall v \in V \tag{8}$$

DOI: 10.1002/nme

Consequently, Equations (7a) and (7b) become

$$\begin{aligned}&\int_\Omega \nabla\delta\bar{u}^h\cdot\nabla\bar{u}^h\mathrm{d}\Omega+\int_\Gamma \delta\bar{u}^h\nabla\hat{u}^h\cdot\boldsymbol{n}\mathrm{d}\Gamma\\&-\int_{\Gamma_g}\left(\delta\bar{u}^h\left(\nabla\left(\bar{u}^h+\hat{u}^h\right)\cdot\boldsymbol{n}-\beta\left(\bar{u}^h+\hat{u}^h\right)\right)+\nabla\delta\bar{u}^h\cdot\boldsymbol{n}\left(\bar{u}^h+\hat{u}^h\right)\right)\mathrm{d}\Gamma\\&=\int_{\Gamma_h}\delta\bar{u}^h h\mathrm{d}\Gamma-\int_{\Gamma_g}\left(-\delta\bar{u}^h\beta g+\nabla\delta\bar{u}^h\cdot\boldsymbol{n}g\right)\mathrm{d}\Gamma\end{aligned}\tag{9a}$$

$$\begin{aligned}&\int_\Omega \nabla\delta\hat{u}^h\cdot\nabla\bar{u}^h\mathrm{d}\Omega+\int_\Gamma \delta\hat{u}^h\nabla\hat{u}^h\cdot\boldsymbol{n}\mathrm{d}\Gamma\\&-\int_{\Gamma_g}\left(\delta\hat{u}^h\left(\nabla\left(\bar{u}^h+\hat{u}^h\right)\cdot\boldsymbol{n}-\beta\left(\bar{u}^h+\hat{u}^h\right)\right)+\nabla\delta\hat{u}^h\cdot\boldsymbol{n}\left(\bar{u}^h+\hat{u}^h\right)\right)\mathrm{d}\Gamma\\&=\int_{\Gamma_h}\delta\hat{u}^h h\mathrm{d}\Gamma-\int_{\Gamma_g}\left(-\delta\hat{u}^h\beta g+\nabla\delta\hat{u}^h\cdot\boldsymbol{n}g\right)\mathrm{d}\Gamma\end{aligned}\tag{9b}$$

The requirement of harmonic property of the non-smooth basis in $\hat{u}^h$ allows the transformation of the domain integral to a boundary integral in (9b). With the consideration of taking the leading terms of the asymptotic solution near the singularity point as the basis functions for the non-smooth part of the solution, we follow from Section 2.2 that $\hat{u}^h=0$ on $\Gamma_g\cap\Gamma_s$ and $\nabla\hat{u}^h\cdot\boldsymbol{n}=0$ on $\Gamma_h\cap\Gamma_s$. The ISBFM Galerkin formulations (9a) and (9b) can be expressed as follows:

$$\begin{aligned}&\int_\Omega \nabla\delta\bar{u}^h\cdot\nabla\bar{u}^h\mathrm{d}\Omega-\int_{\Gamma_g}\left(\delta\bar{u}^h\left(\nabla\bar{u}^h\cdot\boldsymbol{n}-\beta\bar{u}^h\right)+\nabla\delta\bar{u}^h\cdot\boldsymbol{n}\bar{u}^h\right)\mathrm{d}\Gamma\\&+\int_{\bar{\Gamma}_h}\delta\bar{u}^h\nabla\hat{u}^h\cdot\boldsymbol{n}\mathrm{d}\Gamma-\int_{\bar{\Gamma}_g}\left(-\delta\bar{u}^h\beta\hat{u}^h+\nabla\delta\bar{u}^h\cdot\boldsymbol{n}\hat{u}^h\right)\mathrm{d}\Gamma\\&=\int_{\bar{\Gamma}_h}\delta\bar{u}^h h\mathrm{d}\Gamma-\int_{\bar{\Gamma}_g}\left(-\delta\bar{u}^h\beta g+\nabla\delta\bar{u}^h\cdot\boldsymbol{n}g\right)\mathrm{d}\Gamma\end{aligned}\tag{10a}$$

$$\begin{aligned}&\int_{\bar{\Gamma}_h}\nabla\delta\hat{u}^h\cdot\boldsymbol{n}\bar{u}^h\mathrm{d}\Gamma-\int_{\bar{\Gamma}_g}\delta\hat{u}^h\left(\nabla\bar{u}^h\cdot\boldsymbol{n}-\beta\bar{u}^h\right)\mathrm{d}\Gamma\\&+\int_{\bar{\Gamma}_h}\delta\hat{u}^h\nabla\hat{u}^h\cdot\boldsymbol{n}\mathrm{d}\Gamma-\int_{\bar{\Gamma}_g}\left(-\delta\hat{u}^h\beta\hat{u}^h+\nabla\delta\hat{u}^h\cdot\boldsymbol{n}\hat{u}^h\right)\mathrm{d}\Gamma\\&=\int_{\bar{\Gamma}_h}\delta\hat{u}^h h\mathrm{d}\Gamma-\int_{\bar{\Gamma}_g}\left(-\delta\hat{u}^h\beta g+\nabla\delta\hat{u}^h\cdot\boldsymbol{n}g\right)\mathrm{d}\Gamma\end{aligned}\tag{10b}$$

where $\bar{\Gamma}_h=\Gamma_h\backslash\Gamma_s$ and $\bar{\Gamma}_g=\Gamma_g\backslash\Gamma_s$. In the preceding equations, the non-smooth function $\hat{u}^h$ only appears on boundaries away from the singularity point S where the basis functions in $\hat{u}^h$ are actually smooth. The ISBFM Galerkin formulation in (10a) and (10b) can be numerically integrated using lower-order quadrature compared with that of the standard Galerkin formulation in (7a) and (7b). A comparison of the standard and ISBFM Galerkin formulations using different orders of Gauss quadrature rule will be discussed in Section 6.

3.2. Discretization of ISBFM Galerkin formulation

Smooth approximation functions are unable to recover the solution of a singularity problem, whereas adaptive refinement in the vicinity of a singularity can be computationally expensive. In this approach, the RK approximation [15, 16] is employed for the smooth approximation $\bar{u}^h$ in (5) while the leading terms of the asymptotic expansion near the singularity point as given in Table II are used to approximate $\hat{u}^h$.

DOI: 10.1002/nme

The RK approximation of $\bar{u}$, denoted as $\bar{u}^h$, is expressed as

$$\bar{u}^h(\boldsymbol{x}) = \sum_{I=1}^{\bar{N}} \Psi_I(\boldsymbol{x})\bar{d}_I \tag{11}$$

where $\bar{d}_I$ are the coefficients of the approximation, $\bar{N}$ is the number of discrete points, and Ψ_I is the RK shape function expressed as

$$\Psi_I(\boldsymbol{x}) = \boldsymbol{H}^{\mathrm{T}}(\boldsymbol{0})\boldsymbol{M}^{-1}(\boldsymbol{x})\,\boldsymbol{H}(\boldsymbol{x}-\boldsymbol{x}_I)\Phi_a\left(\frac{\|\boldsymbol{x}-\boldsymbol{x}_I\|}{a}\right) \tag{12}$$

with

$$\boldsymbol{M}(\boldsymbol{x}) = \sum_{I=1}^{\bar{N}} \boldsymbol{H}(\boldsymbol{x}-\boldsymbol{x}_I)\boldsymbol{H}^{\mathrm{T}}(\boldsymbol{x}-\boldsymbol{x}_I)\Phi_a\left(\frac{\|\boldsymbol{x}-\boldsymbol{x}_I\|}{a}\right) \tag{13}$$

where $\boldsymbol{x}_I$ is the nodal coordinate, $\boldsymbol{H}^{\mathrm{T}}(\boldsymbol{x}-\boldsymbol{x}_I)$ is the vector containing the complete n-th-order monomial bases to ensure n-th-order completeness in the approximation, $\boldsymbol{M}(\boldsymbol{x})$ is called the moment matrix, and Φ_a is the kernel with compact support a. The kernel function determines the locality and smoothness (order of continuity) of the approximation, for example, the cubic B-spline, Gaussian, and exponential functions. It should be noted that the RK approximation is not an interpolation and the RK shape functions do not possess the Kronecker delta properties. This implies that the imposition of essential boundary conditions needs additional treatment, such as the transformation method [16, 40], enhancing the shape function to recover the Kronecker delta property [41] and Nitsche's method [38, 39].

The approximation of the non-smooth part of the solution $\hat{u}^h$ in (5) is constructed by a linear combination of non-smooth basis functions $\boldsymbol{F}$ as follows

$$\hat{u}^h(x) = \sum_{m=1}^{\hat{N}} F_m(x)\hat{d}_m = \boldsymbol{F}^{\mathrm{T}}(x)\hat{\boldsymbol{d}} \tag{14}$$

where $\hat{N}$ is the number of basis functions F_m as discussed in Section 2.2 and $\hat{d}_m$ is the coefficient of the non-smooth approximation. The non-smooth basis functions are harmonic and satisfy

$$\begin{cases} F_m = 0 & \text{on} \quad \Gamma_g \cap \Gamma_s \\ \nabla F_m \cdot \boldsymbol{n} = 0 & \text{on} \quad \Gamma_h \cap \Gamma_s \end{cases} \tag{15}$$

The properties in (15) enable the ISBFM Galerkin framework presented in Section 3.1.

Substituting (11) and (14) into ISBFM Galerkin equations in (10a) and (10b), the following matrix equation is obtained

$$\boldsymbol{K}\boldsymbol{d} = \begin{bmatrix} \bar{\boldsymbol{K}} & \widehat{\boldsymbol{K}} \\ \widehat{\boldsymbol{K}}^{\mathrm{T}} & \hat{\boldsymbol{K}} \end{bmatrix} \begin{bmatrix} \bar{\boldsymbol{d}} \\ \hat{\boldsymbol{d}} \end{bmatrix} = \begin{bmatrix} \bar{\boldsymbol{f}} \\ \hat{\boldsymbol{f}} \end{bmatrix} = \boldsymbol{f} \tag{16}$$

The stiffness matrix $\boldsymbol{K} \in \mathrm{R}^{N\times N}$ is a positive definite matrix, where $N = \bar{N} + \hat{N}$. The sub-matrix $\bar{\boldsymbol{K}} \in \mathrm{R}^{\bar{N}\times\bar{N}}$ is a sparse matrix, $\widehat{\boldsymbol{K}} \in \mathrm{R}^{\bar{N}\times\hat{N}}$ and $\hat{\boldsymbol{K}} \in \mathrm{R}^{\hat{N}\times\hat{N}}$ are the sub-matrices resulting from (10a) and (10b). The entries of those matrices are given as

$$\bar{K}_{IJ} = \int_\Omega \nabla\Psi_I \cdot \nabla\Psi_J \mathrm{d}\Omega - \int_{\Gamma_g} (\Psi_I \nabla\Psi_J \cdot \boldsymbol{n} + \nabla\Psi_I \cdot \boldsymbol{n}\Psi_J)\,\mathrm{d}\Gamma + \beta\int_{\Gamma_g} \Psi_I\Psi_J \mathrm{d}\Gamma \tag{17}$$

$$\hat{K}_{mn} = \int_{\bar{\Gamma}_h} F_m \nabla F_n \cdot \boldsymbol{n}\mathrm{d}\Gamma - \int_{\bar{\Gamma}_g} \nabla F_m \cdot \boldsymbol{n} F_n \mathrm{d}\Gamma + \beta\int_{\bar{\Gamma}_g} F_m F_n \mathrm{d}\Gamma \tag{18}$$

DOI: 10.1002/nme

and

$$\widehat{K}_{In} = \int_{\bar{\Gamma}_h} \Psi_I \nabla F_n \cdot \boldsymbol{n} \mathrm{d}\Gamma - \int_{\bar{\Gamma}_g} \nabla \Psi_I \cdot \boldsymbol{n} F_n \mathrm{d}\Gamma + \beta \int_{\bar{\Gamma}_g} \Psi_I F_n \mathrm{d}\Gamma \tag{19}$$

The right-hand side vector $\boldsymbol{f} \in \mathrm{R}^{N\times 1}$ in (16) consists of two sub-vectors $\bar{\boldsymbol{f}} \in \mathrm{R}^{\bar{N}\times 1}$ and $\hat{\boldsymbol{f}} \in \mathrm{R}^{\hat{N}\times 1}$ defined as

$$\bar{f}_I = \int_{\bar{\Gamma}_h} \Psi_I h \mathrm{d}\Gamma - \int_{\bar{\Gamma}_g} (-\Psi_I \beta g + \nabla \Psi_I \cdot \boldsymbol{n} g) \mathrm{d}\Gamma \tag{20}$$

and

$$\hat{f}_m = \int_{\bar{\Gamma}_h} F_m h \mathrm{d}\Gamma - \int_{\bar{\Gamma}_g} (-F_m \beta g + \nabla F_m \cdot \boldsymbol{n} g) \mathrm{d}\Gamma \tag{21}$$

The discrete equation of ISBFM Galerkin formulation is used to construct the MOR models in the following section.

4. REDUCED-ORDER MODEL BASED ON ISBFM GALERKIN APPROXIMATION

In this section, we introduce two reduced-order methods for problems with singularity. We consider that the fine-scale solution is obtained based on the ISBFM Galerkin formulation discussed in Section 3.

4.1. Uniform and decomposed model reductions

The general form of a reduced-order model of dimension $k \leqslant N$ is given by

$$\boldsymbol{K}^r \boldsymbol{d}^r = \boldsymbol{f}^r \tag{22}$$

where $\boldsymbol{K}^r \in \mathrm{R}^{k\times k}$ denotes the reduced stiffness matrix, $\boldsymbol{f}^r \in \mathrm{R}^{k\times 1}$ is the reduced force vector, and $\boldsymbol{d}^r \in \mathrm{R}^{k\times 1}$ is the reduced coefficient vector. The reduced system is obtained from a projection of the full system. The fine-scale coefficient vector $\boldsymbol{d}$ in (16) is approximated by

$$\boldsymbol{d} \approx \boldsymbol{P} \boldsymbol{d}^r \tag{23}$$

where $\boldsymbol{P} \in \mathrm{R}^{N\times k}$ is the projection matrix whose columns are orthonormal vectors and $\boldsymbol{d}^r$ is the reduced coefficient vector. We will study two ways of forming the projection matrix using modal analysis.

The first MOR method introduces a uniform reduction (UR) of the fine-scale discrete system constructed from the ISBFM Galerkin formulation, termed ISBFM-UR, where the projection $\boldsymbol{P}^{ur}$ is applied to all DOFs consisting of the smooth and non-smooth parts of the solution. The reduced system is of the form

$$\boldsymbol{K}^{ur} \boldsymbol{d}^{ur} = \boldsymbol{f}^{ur}, \quad \boldsymbol{K}^{ur} = \boldsymbol{P}^{ur\mathrm{T}} \boldsymbol{K} \boldsymbol{P}^{ur}, \quad \boldsymbol{f}^{ur} = \boldsymbol{P}^{ur\mathrm{T}} \boldsymbol{f} \tag{24}$$

where the superscript ur in (24) signifies the UR concept, $\boldsymbol{d}^{ur} \in \mathrm{R}^{k\times 1}$ is the reduced coefficient vector, $\boldsymbol{K}^{ur} \in \mathrm{R}^{k\times k}$ is the reduced stiffness matrix, and $\boldsymbol{f}^{ur} \in \mathrm{R}^{k\times 1}$ is the reduced force vector. The projection matrix $\boldsymbol{P}^{ur}$ is constructed from the orthonormal eigenvectors $\{\boldsymbol{\phi}_i\}_{i=1}^k$ corresponding to the k smallest eigenvalues $\lambda_1 \leqslant \lambda_i \leqslant \lambda_k$ of $\boldsymbol{K}$; that is, $\boldsymbol{P}^{ur} = [\,\boldsymbol{\phi}_1\ \boldsymbol{\phi}_2\ \ldots\ \boldsymbol{\phi}_k\,]$. The components of the reduced-order coefficient vector is $d_i^{ur} = \boldsymbol{\phi}_i^{\mathrm{T}} \boldsymbol{f} \,/\, \lambda_i, i = 1, \ldots, k$, and the approximated fine-scale coefficient vector is obtained from $\boldsymbol{d} \approx \boldsymbol{P}^{ur} \boldsymbol{d}^{ur}$.

The second MOR approach considers decomposed reduction (DR) from the fine-scale system via separate projections for the smooth and non-smooth parts of the fine-scale solution, named ISBFM-DR. Under this approach, the reduced coefficient vector $\boldsymbol{d}^{dr} \in \mathrm{R}^{k\times 1}$ constitutes a reduced

DOI: 10.1002/nme

coefficient vector for the smooth part $\bar{\boldsymbol{d}}^{dr} \in \mathrm{R}^{\bar{k}\times 1}$ and a reduced coefficient vector for the non-smooth part $\hat{\boldsymbol{d}}^{dr} \in \mathrm{R}^{\hat{k}\times 1}$ that are obtained from a decomposed projection matrix with superscript dr denoting the DR approach, given as

$$\boldsymbol{d} \approx \boldsymbol{P}^{dr}\boldsymbol{d}^{dr}, \quad \boldsymbol{P}^{dr} = \begin{bmatrix} \bar{\boldsymbol{P}} & \boldsymbol{0} \\ \boldsymbol{0} & \hat{\boldsymbol{P}} \end{bmatrix} \in \mathrm{R}^{\left(\bar{N}+\hat{N}\right)\times\left(\bar{k}+\hat{k}\right)} \tag{25}$$

where $\bar{\boldsymbol{P}} \in \mathrm{R}^{\bar{N}\times\bar{k}}$ and $\hat{\boldsymbol{P}} \in \mathrm{R}^{\hat{N}\times\hat{k}}$ are the sub-projections for the smooth and non-smooth parts of the fine-scale solution, respectively, and the reduced dimension is $k = \bar{k} + \hat{k}$, with $\bar{k} \leqslant \bar{N}$ and $\hat{k} \leqslant \hat{N}$. The corresponding reduced system is given as

$$\begin{bmatrix} \bar{\boldsymbol{P}}^{\mathrm{T}} & \boldsymbol{0} \\ \boldsymbol{0} & \hat{\boldsymbol{P}}^{\mathrm{T}} \end{bmatrix} \begin{bmatrix} \bar{\boldsymbol{K}} & \widehat{\boldsymbol{K}} \\ \widehat{\boldsymbol{K}}^{\mathrm{T}} & \hat{\boldsymbol{K}} \end{bmatrix} \begin{bmatrix} \bar{\boldsymbol{P}} & \boldsymbol{0} \\ \boldsymbol{0} & \hat{\boldsymbol{P}} \end{bmatrix} \begin{bmatrix} \bar{\boldsymbol{d}}^{dr} \\ \hat{\boldsymbol{d}}^{dr} \end{bmatrix} = \begin{bmatrix} \bar{\boldsymbol{P}}^{\mathrm{T}} & \boldsymbol{0} \\ \boldsymbol{0} & \hat{\boldsymbol{P}}^{\mathrm{T}} \end{bmatrix} \begin{bmatrix} \bar{\boldsymbol{f}} \\ \hat{\boldsymbol{f}} \end{bmatrix} \tag{26}$$

We rewrite the preceding equation as follows

$$\boldsymbol{K}^{dr}\boldsymbol{d}^{dr} = \boldsymbol{f}^{dr} \tag{27}$$

where

$$\boldsymbol{K}^{dr} = \begin{bmatrix} \bar{\boldsymbol{K}}^{dr} & \widehat{\boldsymbol{K}}^{dr} \\ \widehat{\boldsymbol{K}}^{dr\mathrm{T}} & \hat{\boldsymbol{K}}^{dr} \end{bmatrix}, \ \boldsymbol{d}^{dr} = \begin{bmatrix} \bar{\boldsymbol{d}}^{dr} \\ \hat{\boldsymbol{d}}^{dr} \end{bmatrix}, \ \boldsymbol{f}^{dr} = \begin{bmatrix} \bar{\boldsymbol{f}}^{dr} \\ \hat{\boldsymbol{f}}^{dr} \end{bmatrix} \tag{28}$$

Here, $\bar{\boldsymbol{K}}^{dr} = \bar{\boldsymbol{P}}^{\mathrm{T}}\bar{\boldsymbol{K}}\,\bar{\boldsymbol{P}} \in \mathrm{R}^{\bar{k}\times\bar{k}}$, $\widehat{\boldsymbol{K}}^{dr} = \bar{\boldsymbol{P}}^{\mathrm{T}}\,\widehat{\boldsymbol{K}}\,\hat{\boldsymbol{P}} \in \mathrm{R}^{\bar{k}\times\hat{k}}$, and $\hat{\boldsymbol{K}}^{dr} = \hat{\boldsymbol{P}}^{\mathrm{T}}\hat{\boldsymbol{K}}\,\hat{\boldsymbol{P}} \in \mathrm{R}^{\hat{k}\times\hat{k}}$ are the sub-matrices of the reduced stiffness matrix $\boldsymbol{K}^{dr}$, and $\bar{\boldsymbol{f}}^{dr} = \bar{\boldsymbol{P}}^{\mathrm{T}}\bar{\boldsymbol{f}} \in \mathrm{R}^{\bar{k}\times 1}$ and $\hat{\boldsymbol{f}}^{dr} = \hat{\boldsymbol{P}}^{\mathrm{T}}\hat{\boldsymbol{f}} \in \mathrm{R}^{\hat{k}\times 1}$ are the sub-vectors of the reduced force vector $\boldsymbol{f}^{dr}$. We assume that sub-matrices $\hat{K}$ and $\hat{K}^{dr}$ are nonsingular.

In ISBFM-DR, we first solve the coefficient vector of the reduced smooth solution and then compute the reduced coefficient vector of the non-smooth part. Consider the following decomposition of the fine-scale equation in (16)

$$\bar{\boldsymbol{K}}^{c}\bar{\boldsymbol{d}} = \bar{\boldsymbol{f}}^{c}, \ \bar{\boldsymbol{K}}^{c} = \left(\bar{\boldsymbol{K}} - \widehat{\boldsymbol{K}}\,\hat{K}^{-1}\,\widehat{\boldsymbol{K}}^{\mathrm{T}}\right)\bar{\boldsymbol{d}}, \ \bar{\boldsymbol{f}}^{c} = \bar{\boldsymbol{f}} - \widehat{\boldsymbol{K}}\,\hat{K}^{-1}\hat{\boldsymbol{f}} \tag{29a}$$

$$\hat{\boldsymbol{K}}\hat{d} = \hat{\boldsymbol{f}}^{c}, \ \hat{\boldsymbol{f}}^{c} = \hat{\boldsymbol{f}} - \widehat{\boldsymbol{K}}^{\mathrm{T}}\,\bar{\boldsymbol{d}} \tag{29b}$$

The sub-projections matrices $\bar{\boldsymbol{P}}$ and $\hat{\boldsymbol{P}}$ in (25) are respectively obtained from the eigenanalysis of $\bar{\boldsymbol{K}}^{c}$ and $\hat{\boldsymbol{K}}$ from the condensed fine-scale system in (29a) and (29b). That is, $\bar{\boldsymbol{P}} = [\,\bar{\boldsymbol{\varphi}}_1\ \bar{\boldsymbol{\varphi}}_2\ \ldots\ \bar{\boldsymbol{\varphi}}_{\bar{k}}\,]$ and $\hat{\boldsymbol{P}} = [\,\hat{\boldsymbol{\varphi}}_1\ \hat{\boldsymbol{\varphi}}_2\ \ldots\ \hat{\boldsymbol{\varphi}}_{\hat{k}}\,]$, where $\{\bar{\boldsymbol{\varphi}}_j, \bar{\mu}_j\}_{j=1}^{\bar{k}}$ and $\{\hat{\boldsymbol{\varphi}}_l, \hat{\mu}_l\}_{l=1}^{\hat{k}}$ are the smallest eigenpairs from matrices $\bar{\boldsymbol{K}}^{c}$ and $\hat{\boldsymbol{K}}$, respectively. The reduced coefficient vectors are obtained as $\bar{d}_j^{dr} = \bar{\boldsymbol{\varphi}}_j^{\mathrm{T}}\bar{\boldsymbol{f}}^{c} \,/\, \bar{\mu}_j, j = 1,\ldots,\bar{k}$ and $\hat{d}_l^{dr} = \hat{\boldsymbol{\varphi}}_l^{\mathrm{T}}\hat{\boldsymbol{f}}^{cdr} \,/\, \hat{\mu}_l, l = 1,\ldots,\hat{k}$, where $\hat{\boldsymbol{f}}^{cdr} = \hat{\boldsymbol{f}} - \widehat{\boldsymbol{K}}^{\mathrm{T}}\,\bar{\boldsymbol{P}}\bar{\boldsymbol{d}}^{dr}$. The approximation from the reduced-order solution is then obtained as $\boldsymbol{d}^{\mathrm{T}} \approx [[\bar{\boldsymbol{P}}\bar{\boldsymbol{d}}^{dr}]^{\mathrm{T}}, [\hat{\boldsymbol{P}}\hat{\boldsymbol{d}}^{dr}]^{\mathrm{T}}]$.

Remark 4.1

If the non-smooth DOF is relatively small compared with the number of smooth DOF, one can consider reducing the smooth DOF of the solution only and keeping the non-smooth DOF unprojected. That is, in the ISBFM-DR method, the dimension $\hat{k} = \hat{N}$ and $\hat{\boldsymbol{P}} = \boldsymbol{I}_{\hat{N}}$, and $\hat{\boldsymbol{d}}^{dr} \in \mathrm{R}^{\hat{N}\times 1}$ is obtained directly from $\hat{\boldsymbol{K}}\hat{\boldsymbol{d}}^{dr} = \hat{\boldsymbol{f}}^{cdr}$.

DOI: 10.1002/nme

Table III. Operation counts.

Procedure	Operation counts (op)
Block Cholesky	$\frac{\bar{N}^3-\hat{N}^3}{6}+2\bar{N}\hat{N}^2+\hat{N}^2+N^2$
ISBFM-UR	$(4p+6k+9+\gamma)pN$ $+2k^2N+(k+p)^3$ $+(N+1)k+kN$
ISBFM-DR	$\left(4\bar{p}+6\bar{k}+9+\bar{\gamma}\right)\bar{p}\bar{N}$ $+2\bar{k}^2\bar{N}+\left(\bar{k}+\bar{p}\right)^3$ $+\left(4\hat{p}+6\hat{k}+9+\hat{\gamma}\right)\hat{p}\hat{N}$ $+2\hat{k}^2\hat{N}+\left(\hat{k}+\hat{p}\right)^3$ $+2\hat{N}^2+\bar{N}\hat{N}^2+\bar{N}^2\hat{N}+\bar{N}^2$ $+2\bar{N}\hat{N}+\bar{N}+\hat{N}$ $+2\bar{k}\bar{N}+2\hat{k}\hat{N}+\bar{k}+\hat{k}$

4.2. Operation counts of reduced model

The total operation counts in applying each of the two proposed MOR methods are presented in this section and are compared with the operation count in solving the fine-scale system. We assume that the full solution is obtained when block Cholesky factorization is applied to (16). In this work, we use the implicitly restarted Lanczos method [42–44] to obtain the approximate eigenpairs. The operation counts (op) for the two proposed MOR methods are obtained using additions/subtractions (A/S) and multiplications/divisions (M/D) comparisons [45, 46], where

$$1(\text{op}) : 1(\text{A/S}) + 1(\text{M/D}) \tag{30}$$

The operational counts for solving the full system, ISBFM-UR, and ISBFM-DR are listed in Table III.

In Table III, the Schur complement is considered in block Cholesky factorization, and the parameter γ is twice the average number of non-zero entries per row of matrix $\boldsymbol{K}$ in (16), $\bar{\gamma}$ is twice the average number of non-zero entries per row of matrix $\bar{\boldsymbol{K}}^c$ in (29a), and $\hat{\gamma}$ is twice the average number of non-zero entries per row of $\hat{\boldsymbol{K}}$. The parameter p is the number of steps in the Lanczos method for ISBFM-UR, and $\bar{p}$ and $\hat{p}$ are the numbers of steps in Lanczos methods used in ISBFM-DR.

It appears that the cost in ISBFM-DR is slightly lower than that in ISBFM-UR from the fact that $\bar{k}^2+\hat{k}^2<k^2$ and $\bar{k}^3+\hat{k}^3<k^3$. Both of these MOR approaches are more efficient than solving the fine-scale system directly, owing to the fact that $\bar{N}^2<N^3$ and $\hat{N}^2<N^3$.

5. ASSESSMENT OF ERROR AND STABILITY OF THE REDUCED-ORDER MODELS

In this section, the error bound and stability analysis of the two proposed MOR methods are given.

5.1. Error bounds estimation

For ISBFM-UR, let $\boldsymbol{\Phi}^{\mathrm{T}}=\left\{\boldsymbol{\Psi}^{\mathrm{T}},\boldsymbol{F}^{\mathrm{T}}\right\}$ be the collection of RK shape functions and non-smooth basis functions, and let $\boldsymbol{\Phi}^{ur\mathrm{T}}$ be the projected basis functions from fine-scale basis functions $\boldsymbol{\Phi}^{\mathrm{T}}$; that is, $\boldsymbol{\Phi}^{ur\mathrm{T}}=\boldsymbol{\Phi}^{\mathrm{T}}\boldsymbol{P}^{ur}$. It follows that the reduced solution is $u^{ur}=\boldsymbol{\Phi}^{ur\mathrm{T}}\boldsymbol{d}^{ur}$. The solution error in vector sup-norm between the full model and the reduced model is given by

DOI: 10.1002/nme

$$\begin{aligned}\left\|u^h - u^{ur}\right\|_\infty &= \left\|\boldsymbol{\Phi}^{\mathrm{T}}\boldsymbol{d} - \boldsymbol{\Phi}^{ur\mathrm{T}}\boldsymbol{d}^{ur}\right\|_\infty \\ &\leqslant \|\boldsymbol{\Phi}\|_\infty \|\boldsymbol{d} - \boldsymbol{P}^{ur}\boldsymbol{d}^{ur}\|_\infty \\ &\leqslant \|\boldsymbol{\Phi}\|_\infty \max_{i\in G}\left|\frac{\boldsymbol{\phi}_i^{\mathrm{T}}\boldsymbol{f}}{\lambda_i}\right|\end{aligned} \tag{31}$$

where $G = \{k+1,\ldots,N\}$ is a set of indices of the eigenpairs $\{\boldsymbol{\phi}_i,\lambda_i\}_{i=1}^N$ satisfying the eigensystem $\boldsymbol{K}\boldsymbol{\phi}_i = \lambda_i\boldsymbol{\phi}_i$ that have been truncated in the projection to the reduced system.

By using the Schwarz inequality and the pairwise orthonormal eigenvectors, we have

$$\max_{i\in G}\left|\frac{\boldsymbol{\phi}_i^{\mathrm{T}}\boldsymbol{f}}{\lambda_i}\right| \leqslant \sqrt{N}\frac{\|\boldsymbol{f}\|_\infty}{\lambda_{k+1}} \tag{32}$$

where λ_{k+1} is the smallest eigenvector beyond the selected eigenpairs $\{\boldsymbol{\phi}_i,\lambda_i\}_{i=1}^k$ that form the projection matrix. The error bound for the ISBFM-UR is expressed as

$$\left\|u^h - u^{ur}\right\|_\infty \leqslant \sqrt{N}\lambda_{k+1}^{-1}\|\boldsymbol{\Phi}\|_\infty\|\boldsymbol{f}\|_\infty \tag{33}$$

It can be observed that the solution error is related to the smallest remaining eigenvalues not considered in the construction of the projection $\boldsymbol{P}^{ur}$. Note that the error bound in (33) would vary when different numerical techniques for the imposition of boundary conditions are used.

Next, we present the error estimation for ISBFM-DR. From the fine-scale model decoupled in (29a) and (29b), we have

$$\boldsymbol{d} = \hat{\boldsymbol{K}}^{-1}\hat{\boldsymbol{f}}^c = \hat{\boldsymbol{K}}^{-1}\left(\hat{\boldsymbol{f}} - \widehat{\boldsymbol{K}}^{\mathrm{T}}\bar{\boldsymbol{d}}\right) \tag{34}$$

The reduced system (27) can be decoupled similarly. After solving the coefficient vector of the smooth part $\bar{\boldsymbol{d}}^{dr}$, the coefficient vector of non-smooth part $\hat{\boldsymbol{d}}^{dr}$ can be obtained as well; that is,

$$\hat{\boldsymbol{d}}^{dr} = \left(\hat{\boldsymbol{K}}^{dr}\right)^{-1}\left(\hat{\boldsymbol{f}}^{dr} - \widehat{\boldsymbol{K}}^{dr\mathrm{T}}\bar{\boldsymbol{d}}^{dr}\right) = \hat{\boldsymbol{P}}^{+}\hat{\boldsymbol{K}}^{-1}\left(\hat{\boldsymbol{f}} - \widehat{\boldsymbol{K}}^{\mathrm{T}}\bar{\boldsymbol{P}}\bar{\boldsymbol{d}}^{dr}\right) \tag{35}$$

where $\hat{\boldsymbol{P}}^{+}$ is the pseudo-inverse of non-square matrix $\hat{\boldsymbol{P}}$. By subtracting $\hat{\boldsymbol{P}}$ times (35) from (34), it follows that

$$\hat{\boldsymbol{d}} - \hat{\boldsymbol{P}}\hat{\boldsymbol{d}}^{dr} = \hat{\boldsymbol{K}}^{-1}\widehat{\boldsymbol{K}}^{\mathrm{T}}\left(\bar{\boldsymbol{P}}\bar{\boldsymbol{d}}^{dr} - \bar{\boldsymbol{d}}\right) \tag{36}$$

In a similar way, we have the error estimation for ISBFM-DR as follows:

$$\begin{aligned}\left\|u^h - u^{dr}\right\|_\infty &= \left\|\boldsymbol{\Psi}^{\mathrm{T}}\bar{\boldsymbol{d}} + \boldsymbol{F}^{\mathrm{T}}\hat{\boldsymbol{d}} - \left(\boldsymbol{\Psi}^{\mathrm{T}}\bar{\boldsymbol{P}}\bar{\boldsymbol{d}}^{dr} + \boldsymbol{F}^{\mathrm{T}}\hat{\boldsymbol{P}}\hat{\boldsymbol{d}}^{dr}\right)\right\|_\infty \\ &\leqslant \|\boldsymbol{\Psi}\|_\infty\left\|\bar{\boldsymbol{d}} - \bar{\boldsymbol{P}}\bar{\boldsymbol{d}}^{dr}\right\|_\infty + \|\boldsymbol{F}\|_\infty\left\|\hat{\boldsymbol{d}} - \hat{\boldsymbol{P}}\hat{\boldsymbol{d}}^{dr}\right\|_\infty \\ &\leqslant \left\{\|\boldsymbol{\Psi}\|_\infty + \|\boldsymbol{F}\|_\infty\left\|\hat{\boldsymbol{K}}^{-1}\widehat{\boldsymbol{K}}^{\mathrm{T}}\right\|_\infty\right\}\left\|\bar{\boldsymbol{d}} - \bar{\boldsymbol{P}}\bar{\boldsymbol{d}}^{dr}\right\|_\infty\end{aligned} \tag{37}$$

We can estimate the order of $\|\hat{\boldsymbol{K}}^{-1}\ \widehat{\boldsymbol{K}}^{\mathrm{T}}\|_\infty$ from the definition of entries of sub-matrices in Section 3.2 and from the properties of RK shape functions, $\|\Psi_I\|_\infty \leqslant C$ and $\|\nabla\Psi_I\|_\infty \leqslant Ca^{-1}$, where a is the support size of the kernel function. We also consider the regularity of non-smooth basis functions to yield

$$\left[\hat{\boldsymbol{K}}^{-1}\widehat{\boldsymbol{K}}^{\mathrm{T}}\right]_{IJ} \approx O\left(r^{-\alpha_I}\right) \tag{38}$$

DOI: 10.1002/nme

where $I = 1, \ldots, \hat{N}$ and

$$\alpha_I = \begin{cases} 2I/3 & \text{for } \Theta = 3\pi/2 \\ I - 1/2 & \text{for } \Theta = 2\pi \end{cases} \tag{39}$$

Consequently, we have a bound as follows:

$$\left\| \hat{\boldsymbol{K}}^{-1} \, \widehat{\boldsymbol{K}}^{\mathrm{T}} \right\|_{\infty} \leqslant \hat{C} \tag{40}$$

where $\hat{C}$ is a bounded constant. Equation (37) is further manipulated to yield

$$\begin{aligned} \left\| u^h - u^{dr} \right\|_{\infty} &\leqslant \left(\|\boldsymbol{\Psi}\|_{\infty} + \hat{C} \|\boldsymbol{F}\|_{\infty} \right) \left\| \bar{\boldsymbol{d}} - \bar{\boldsymbol{P}} \bar{\boldsymbol{d}}^{dr} \right\|_{\infty} \\ &\leqslant \sqrt{\bar{N}} \bar{\mu}_{\bar{k}+1}^{-1} \left(C + \hat{C} \|\boldsymbol{F}\|_{\infty} \right) \left\| \bar{\boldsymbol{f}}^{c} \right\|_{\infty} \end{aligned} \tag{41}$$

where $\bar{G} = \left\{ \bar{k} + 1, \ldots, \bar{N} \right\}$ is the set of indices of the selected eigenpairs $\{\bar{\boldsymbol{\varphi}}_j, \bar{\mu}_j\}_{j=1}^{\bar{N}}$ associated with the eigensystem $\bar{\boldsymbol{K}}^{c} \bar{\boldsymbol{\varphi}}_j = \bar{\mu}_j \bar{\boldsymbol{\varphi}}_j$ that are truncated in the construction of the projection matrix $\bar{\boldsymbol{P}}$.

By inclusion principle and interlacing properties [47], we have the relationship between two sets of eigenvalues $\{\lambda_i\}$and $\{\bar{\mu}_j\}$ for $\boldsymbol{K}$ and $\bar{\boldsymbol{K}}^{c}$, respectively, as follows:

$$\bar{\mu}_i < \lambda_{i+\hat{k}}, \quad \forall i \in \left\{ 1, 2, \ldots, \bar{N} \right\} \tag{42}$$

We have the property that $\bar{\mu}_{\bar{k}+1} < \lambda_{k+1}$ and that the values λ_{k+1} and $\bar{\mu}_{\bar{k}+1}$ are very close when the number of non-smooth basis functions $\hat{N}$ is small. The magnitudes of $\|\boldsymbol{\Phi}\|_{\infty}$ and $\hat{C}\|\boldsymbol{F}\|_{\infty}$ are dependent on the number of non-smooth basis functions used and are usually bounded.

In summary, we have error bounds for ISBFM-UR and ISBFM-DR as follows:

$$\left\| u^h - u^{ur} \right\|_{\infty} \leqslant C_1 \sqrt{N} \lambda_{k+1}^{-1} \|\boldsymbol{f}\|_{\infty} \tag{43}$$

$$\left\| u^h - u^{dr} \right\|_{\infty} \leqslant C_2 \sqrt{\bar{N}} \bar{\mu}_{\bar{k}+1}^{-1} \left\| \bar{\boldsymbol{f}}^{c} \right\|_{\infty} \tag{44}$$

where $C_1 = \|\boldsymbol{\Phi}\|_{\infty}$ and $C_2 = C + \hat{C}\|\boldsymbol{F}\|_{\infty}$. This estimate suggests that the errors of the proposed reduced approximations are greatly influenced by the values of $\|\boldsymbol{f}\|_{\infty}$ and $\|\bar{\boldsymbol{f}}^{c}\|_{\infty}$. The comparison of numerical results with these error analyses is presented in Section 6.

5.2. *Stability analysis*

In this section, the stability of the discrete systems obtained from both ISBFM-UR and ISBFM-DR approaches is studied. We first address the perturbation properties of the reduced system $\boldsymbol{K}^r \boldsymbol{d}^r = \boldsymbol{f}^r$. If both matrix and right-hand-side vector are perturbed, then the solution of reduced system may be expressed as $\boldsymbol{d}^r + \delta \boldsymbol{d}^r$ and satisfies the following equation:

$$\left(\boldsymbol{K}^r + \delta \boldsymbol{K}^r \right) \left(\boldsymbol{d}^r + \delta \boldsymbol{d}^r \right) = \left(\boldsymbol{f}^r + \delta \boldsymbol{f}^r \right) \tag{45}$$

The following relative perturbation bound relates the perturbation of the solution to the perturbation of the left-hand side matrix and the right-hand side vector as

$$\frac{\|\delta \boldsymbol{d}^r\|}{\|\boldsymbol{d}^r\|} \leqslant \frac{\left(1 + \dfrac{\|\delta \boldsymbol{f}^r\|}{\|\boldsymbol{f}^r\|} \right) \dfrac{\|\delta \boldsymbol{K}^r\|}{\|\boldsymbol{K}^r\|} + \operatorname{cond}(\boldsymbol{K}^r) \dfrac{\|\delta \boldsymbol{f}^r\|}{\|\boldsymbol{f}^r\|}}{1 - \left(\dfrac{\|\delta \boldsymbol{K}^r\|^2}{\|\boldsymbol{K}^r\|^2} + (1 + \operatorname{cond}(\boldsymbol{K}^r)) \dfrac{\|\delta \boldsymbol{K}^r\|}{\|\boldsymbol{K}^r\|} \right)} \tag{46}$$

DOI: 10.1002/nme

Herein, the vector 2-norm is considered; that is, $\|\cdot\| = \|\cdot\|_2$; and the condition number is defined as

$$\text{cond}(\boldsymbol{K}^r) = \|\boldsymbol{K}^r\| \left\|(\boldsymbol{K}^r)^{-1}\right\| = \frac{\lambda_{\max}(\boldsymbol{K}^r)}{\lambda_{\min}(\boldsymbol{K}^r)} \tag{47}$$

We can observe from (46) that this condition number plays a key role in the sensitivity of the solution to small perturbations. If the left-hand side matrix is not perturbed, that is $\delta\boldsymbol{K}^r = 0$, then the bound in (46) becomes

$$\frac{\|\delta\boldsymbol{d}^r\|}{\|\boldsymbol{d}^r\|} \leqslant \text{cond}(\boldsymbol{K}^r)\,\frac{\|\delta\boldsymbol{f}^r\|}{\|\boldsymbol{f}^r\|} \tag{48}$$

In the following, we investigate the relation between condition numbers of the full system (16) and the reduced system (22). It can be easily derived that

$$\begin{aligned} \text{cond}(\boldsymbol{K}^r) &= \text{cond}\left(\boldsymbol{P}^{\mathrm{T}}\boldsymbol{K}\boldsymbol{P}\right) \\ &= \left\|\boldsymbol{P}^{\mathrm{T}}\boldsymbol{K}\boldsymbol{P}\right\| \left\|\left(\boldsymbol{P}^{\mathrm{T}}\boldsymbol{K}\boldsymbol{P}\right)^{-1}\right\| \\ &\leqslant \left\|\boldsymbol{P}^{\mathrm{T}}\right\| \|\boldsymbol{K}\| \|\boldsymbol{P}\| \left\|\boldsymbol{P}^{+}\right\| \left\|\boldsymbol{K}^{-1}\right\| \left\|\left(\boldsymbol{P}^{\mathrm{T}}\right)^{+}\right\| \\ &\leqslant \|\boldsymbol{K}\| \left\|\boldsymbol{K}^{-1}\right\| = \text{cond}(\boldsymbol{K}) \end{aligned} \tag{49}$$

In the preceding inequality, $\|\boldsymbol{P}\| = \|\boldsymbol{P}^T\| = 1$ has been considered, as the matrix $\boldsymbol{P}$ has orthonormal columns.

Next, we consider the reduced matrix $\boldsymbol{K}^r$ in (22) obtained from the two MOR methods:

(i) ISBFM-UR: $\boldsymbol{K}^r = \boldsymbol{K}^{ur}$ given in (24), where the projection $\boldsymbol{P}^{ur}$ is obtained from $\boldsymbol{K}$ with the eigenpairs $\{\boldsymbol{\phi}, \lambda_i\}_{i=1}^{N}$
(ii) ISBFM-DR: $\boldsymbol{K}^r = \boldsymbol{K}^{dr}$ given in (28), where the sub-projections $\bar{\boldsymbol{P}}$ and $\hat{\boldsymbol{P}}$ are constructed based on $\bar{\boldsymbol{K}}^c$ and $\hat{\boldsymbol{K}}$ with the eigenpairs $\{\bar{\boldsymbol{\varphi}}_j, \bar{\mu}_j\}_{j=1}^{\bar{N}}$ and $\{\hat{\boldsymbol{\varphi}}_l, \hat{\mu}_l\}_{l=1}^{\hat{N}}$, respectively, for the decomposed smooth and non-smooth discrete equations.

By means of the Rayleigh quotient [47] of the reduced stiffness matrix $\boldsymbol{K}^r$, we can derive the bound of condition number for both ISBFM-UR and ISBFM-DR. For ISBFM-UR, the condition number is given by

$$\text{cond}(\boldsymbol{K}^{ur}) = \frac{\lambda_k^{ur}}{\lambda_1^{ur}} = \frac{\lambda_k}{\lambda_1} \tag{50}$$

where $\{\lambda_i^{ur}\}_{i=1}^{k}$ are the eigenvalues of $\boldsymbol{K}^{ur}$. For ISBFM-DR, after some manipulations of the Rayleigh quotient, a bound of the condition number is obtained using eigenvalues of sub-matrices of $\boldsymbol{K}$ as

$$\text{cond}\left(\boldsymbol{K}^{dr}\right) = \frac{\lambda_k^{dr}}{\lambda_1^{dr}} \leqslant \frac{\bar{\mu}_{\bar{k}} + \hat{\mu}_{\hat{k}} + \varepsilon_N}{\lambda_1} \tag{51}$$

where $\{\lambda_i^{dr}\}_{i=1}^{k}$ are the eigenvalues of $\boldsymbol{K}^{dr}$, which are bounded by the minimum and maximum eigenvalues of $\boldsymbol{K}$, that is, $\lambda_1 \leqslant \lambda_i^{dr} \leqslant \lambda_N$, $\forall i \in \{1, 2, \ldots, k\}$. We can deduce the property $\lambda_1 \leqslant \lambda_i^{dr}$. We further define ε_N as the maximal eigenvalue of matrix $\boldsymbol{K}'$ defined as follows:

$$\boldsymbol{K}' := \begin{bmatrix} \widehat{\boldsymbol{K}}\,\hat{\boldsymbol{K}}^{-1}\,\widehat{\boldsymbol{K}}^{\mathrm{T}}\,\widehat{\boldsymbol{K}} & \\ & \widehat{\boldsymbol{K}}^{\mathrm{T}} \quad \boldsymbol{0} \end{bmatrix} \tag{52}$$

The values of ε_N and $\hat{\mu}_{\hat{k}}$ are dependent on the type and the number of non-smooth basis functions used. From the interlacing property in (42), we obtain the relationship between the condition numbers of the reduced systems from ISBFM-UR and ISBFM-DR as follows:

DOI: 10.1002/nme

$$\text{cond}\left(\boldsymbol{K}^{dr}\right) \leqslant \frac{\bar{\mu}_{\bar{k}}}{\lambda_1} + \frac{\hat{\mu}_{\hat{k}} + \varepsilon_N}{\lambda_1} \leqslant \frac{\lambda_k}{\lambda_1} + \frac{\hat{\mu}_{\hat{N}} + \varepsilon_N}{\lambda_1} \leqslant \text{cond}(\boldsymbol{K}^{ur}) + \text{B} \tag{53}$$

where the term $\text{B} > 0$ is affected by the value of $\hat{\mu}_{\hat{N}}$ due to the use of non-smooth basis functions.

From the analytical analysis of the stability for these two reduced systems, we can conclude that the ISBFM-DR has a larger bound of condition number than that in ISBFM-UR. The detail of the eigenspectrum of the different matrices will be presented for the numerical examples studied in Section 6.

6. NUMERICAL EXAMPLES AND DISCUSSIONS

In the following numerical examples, we demonstrate the effectiveness of the proposed ISBFM-UR and ISBFM-DR methods. We first consider an example that identifies the performance of ISBFM Galerkin for a problem with singularity, followed by verification of ISBFM-UR and ISBFM-DR for Poisson problems with mild and strong singularities. In the following study, RK functions using linear basis and cubic B-spline kernel function with a normalized support size of $a = 1.51$ are chosen for the smooth part of the solution. The non-smooth basis functions described in Section 2 are employed to represent the singularities in the solution. For Nitsche's treatment of essential boundary conditions, $\beta = 100/h$ is adopted, where h is the minimal spacing of RK nodes.

6.1. *Comparison of standard Galerkin and ISBFM Galerkin methods in a cracked beam Poisson problem*

To compare the approximated solutions obtained from standard Galerkin and ISBFM Galerkin formulations, we study a two-dimensional cracked beam Poisson problem as shown in Figure 3 in which the discontinuity of boundary condition at $(0, 0)$ yields a singularity of order $\alpha = 1/2$; according to Table I.

The problem statement of the cracked beam Poisson problem is given as

$$\begin{aligned} \Delta u &= 0 \quad \text{in} \quad \Omega \\ u|_{y=0,-1/2\leqslant x\leqslant 0} &= 0,\ u|_{y=1/2,-1/2\leqslant x\leqslant 1/2} = 0.125 \\ \left.\frac{\partial u}{\partial y}\right|_{y=0,0\leqslant x\leqslant 1/2} &= 0,\ \left.\frac{\partial u}{\partial x}\right|_{x=1/2,0\leqslant y\leqslant 1/2} = 0,\ \left.\frac{\partial u}{\partial x}\right|_{x=-1/2,0\leqslant y\leqslant 1/2} = 0 \end{aligned} \tag{54}$$

where $\Omega = (-1/2, 1/2) \times (0, 1/2)$. The non-smooth basis functions of this problem are chosen from the harmonic near-tip functions presented in Table II with N–D type of boundary conditions and $\Theta = \pi$,

$$F_m(r, \theta) = r^{\frac{2m-1}{2}} \cos\left(\frac{2m-1}{2}\theta\right),\ m = 1, 2, \ldots \tag{55}$$

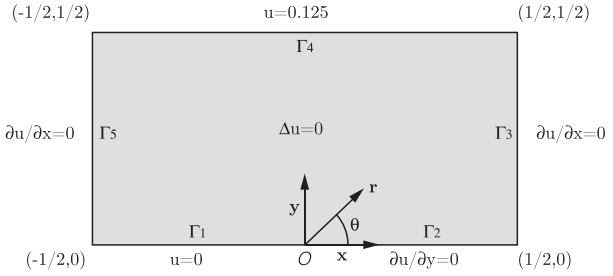

Figure 3. Model of cracked beam problem.

DOI: 10.1002/nme

where $r = \sqrt{(x - x_0)^2 + (y - y_0)^2}$ and $\theta = \tan^{-1}((y - y_0) / (x - x_0))$, which also possess the properties $F_m = 0$ on Γ_1 and $\frac{\partial F_m}{\partial y} = 0$ on Γ_2 near the singularity point (x_0, y_0).

For the assessment of convergence, the normalized errors in L_2 and H^1 norms are considered as follows:

$$e_0 = \frac{\|u - u^h\|_{L_2}}{\|u\|_{L_2}}, \; e_1 = \frac{\|u - u^h\|_{H^1}}{\|u\|_{H^1}} \tag{56}$$

The solution errors of standard Galerkin and ISBFM Galerkin formulations obtained by using a 48×24 uniform discretization with one non-smooth basis function ($\hat{N} = 1$) are shown in Figures 4 and 5, where different orders of the Gauss quadrature rule for the domain and boundary integrals have been used. The results indicate that, for the same Gauss quadrature rule, the solution from ISBFM Galerkin formulation provides better accuracy in both L_2 and H^1 norms. The distributions of the absolute errors of solutions over the domain are compared in Figure 6 where an eighth-order of Gauss quadrature rule has been used in the Galerkin equations to properly integrate non-smooth functions. The error from the standard Galerkin formulation is localized around the singularity point and is much bigger than the error from the ISBFM Galerkin method.

The convergence of standard and ISBFM Galerkin formulations in normalized L_2 error norm is shown in Figure 7 using different numbers of Gauss points (GP) in the quadrature rule. The

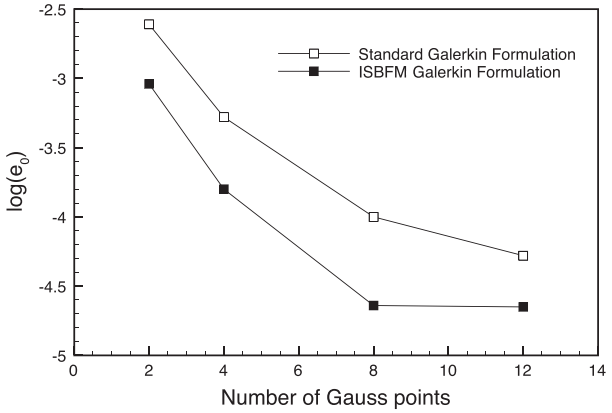

Figure 4. Normalized L_2 error norm in the cracked beam Poisson problem using different Galerkin formulations and different orders of Gauss quadrature. ISBFM, integrated singular basis function method.

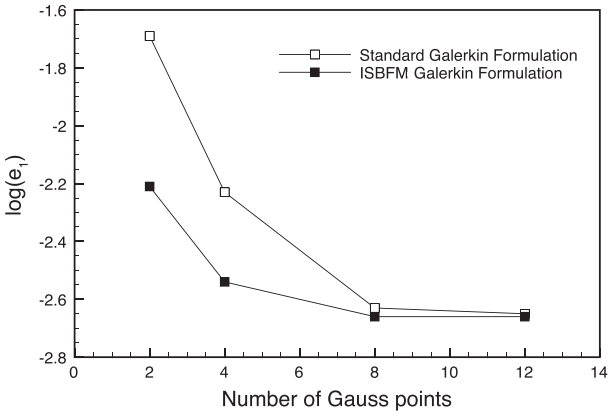

Figure 5. Normalized H^1 error norm in the cracked beam Poisson problem using different Galerkin formulations and different orders of Gauss quadrature. ISBFM, integrated singular basis function method.

DOI: 10.1002/nme

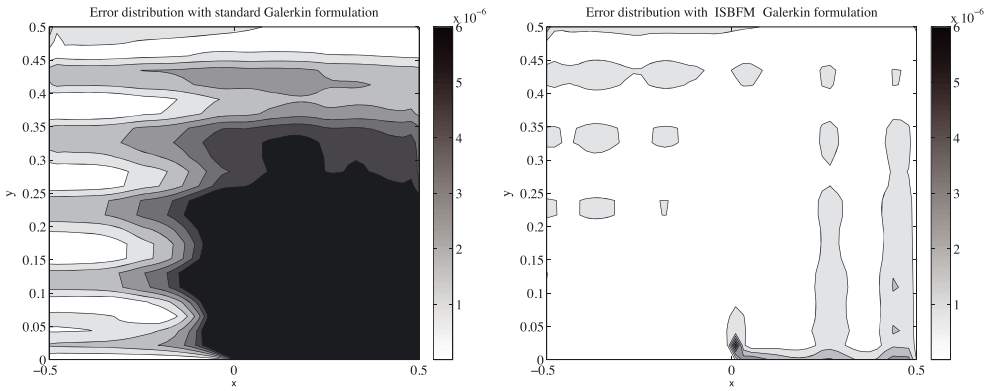

Figure 6. Absolute error distribution of solutions from standard Galerkin and integrated singular basis function method (ISBFM) Galerkin formulations.

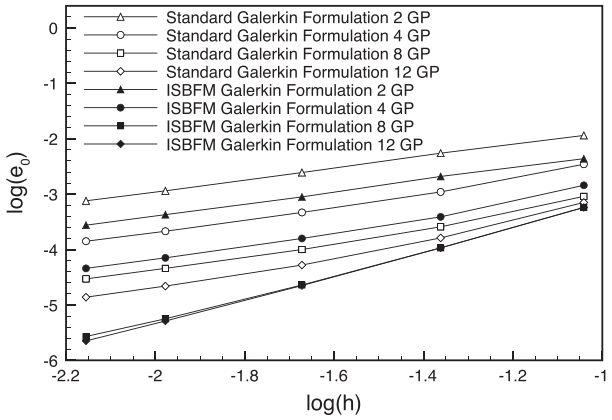

Figure 7. Convergence plot in normalized L_2 error norm of standard Galerkin and ISBFM Galerkin formulations with different orders of Gauss quadrature.

Table IV. Rate of convergence in L_2 norm of standard Galerkin and integrated singular basis function method (ISBFM) Galerkin formulations with different orders of Gauss quadrature.

	Standard Galerkin				ISBFM Galerkin			
Order of Gauss quadrature	2	4	8	12	2	4	8	12
Rate of convergence	1.03	1.05	1.06	1.12	1.04	1.08	1.80	2.04

asymptotic rates of convergence of the approximation are presented in Table IV. The ISBFM Galerkin formulation improves the accuracy of the approximation and also the rate of convergence.

This cracked beam Poisson problem demonstrates that the ISBFM Galerkin method provides a more accurate approximation compared with the standard Galerkin method and allows using a lower order of Gauss quadrature for problems with singularities. The ISBFM Galerkin formulation is also well suited for the proposed MOR approaches, as the singularity behavior is better preserved than that of the standard Galerkin formulation in constructing the reduced-order space.

6.2. Reduced-order modeling of an L-shaped Poisson problem

6.2.1. Problem statement and numerical results. In the following example, the proposed ISBFM-UR and ISBFM-DR methods are considered for the reduced-order modeling of a Poisson problem

DOI: 10.1002/nme

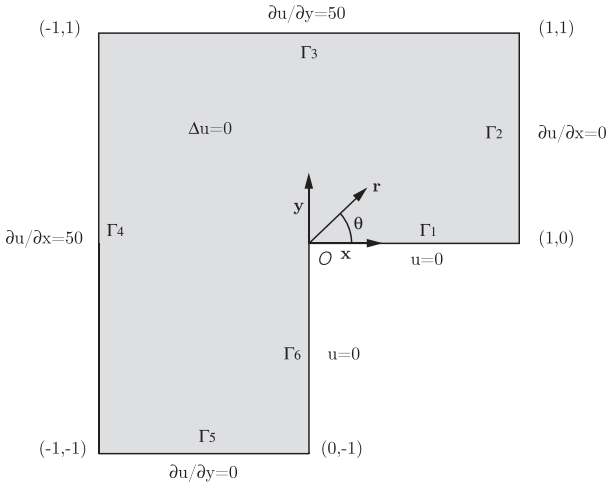

Figure 8. Model of the L-shaped Poisson problem.

with mild singularity, shown in Figure 8. The problem statement of this L-shaped Poisson problem is given as follows:

$$\begin{gathered}\Delta u = 0 \quad \text{in} \quad \Omega \\ u|_{x=0,\,-1\leqslant y\leqslant 0} = 0,\; u\big|_{y=0,0\leqslant x\leqslant 1} = 0 \\ \frac{\partial u}{\partial y}\Big|_{y=-1,\,-1\leqslant x\leqslant 0} = 0,\; \frac{\partial u}{\partial x}\Big|_{x=1,\,0\leqslant y\leqslant 1} = 0,\; \frac{\partial u}{\partial y}\Big|_{y=1,\,-1\leqslant x\leqslant 1} = 50,\; \frac{\partial u}{\partial x}\Big|_{x=-1,\,-1\leqslant y\leqslant 1} = 50\end{gathered} \tag{57}$$

where $\Omega = (-1,1)\times(-1,1)\backslash(0,1)\times(-1,0)$.

The ISBFM-DR method is introduced with order reduction only on the smooth solution, and no order reduction on the enriched solution; that is, $\hat{\boldsymbol{P}} = \boldsymbol{I}_{\hat{N}}$ and $k = \bar{k} + \hat{N}$. The normalized errors in L_∞, L_2, and H^1 norms between the reduced solution u^r and the full solution u^h given in the following are considered in the accuracy assessment of the reduced models:

$$e_\infty = \frac{\|u^h - u^r\|_{L_\infty}}{\|u^h\|_{L_\infty}},\; e_0 = \frac{\|u^h - u^r\|_{L_2}}{\|u^h\|_{L_2}},\; e_1 = \frac{\|u^h - u^r\|_{H^1}}{\|u^h\|_{H^1}} \tag{58}$$

The harmonic functions shown in the following are obtained from Table II with a D–D type of boundary conditions and $\Theta = 3\,/\,2\pi$ and are used as non-smooth basis functions:

$$F_m(r,\theta) = r^{\frac{2}{3}m}\sin\left(\frac{2}{3}m\theta\right),\; m = 1,2,\ldots \tag{59}$$

The non-smooth basis functions satisfy $F_m = 0$ on Γ_6 and $F_m = 0$ on Γ_1 near the singularity point $(0,0)$ according to (57). In this numerical example, the fine-scale solution is obtained for a uniform discretization 49×49 ($\bar{N} = 1825$) with one non-smooth basis function ($\hat{N} = 1$).

The approximated solution of the fine-scale model and its derivatives along $y = 0.001$ are shown in Figure 9. A comparison of the absolute error along $y = 0.001$ between the fine-scale solution and the approximated reduced solutions obtained from ISBFM-UR and ISBFM-DR for various reduced dimensions k, where $k\,/\,N = 5\%,\ 10\%,\ 20\%$, is presented in Figure 10. We first observe that the ISBFM-UR method approximates the fine-scale solution poorly even when using a reduced model with 20% of the full DOF. On the other hand, the reduced-order solution from ISBFM-DR yields a much smaller error, especially in the derivatives of the solution, where the error near the singularity point is not significant.

DOI: 10.1002/nme

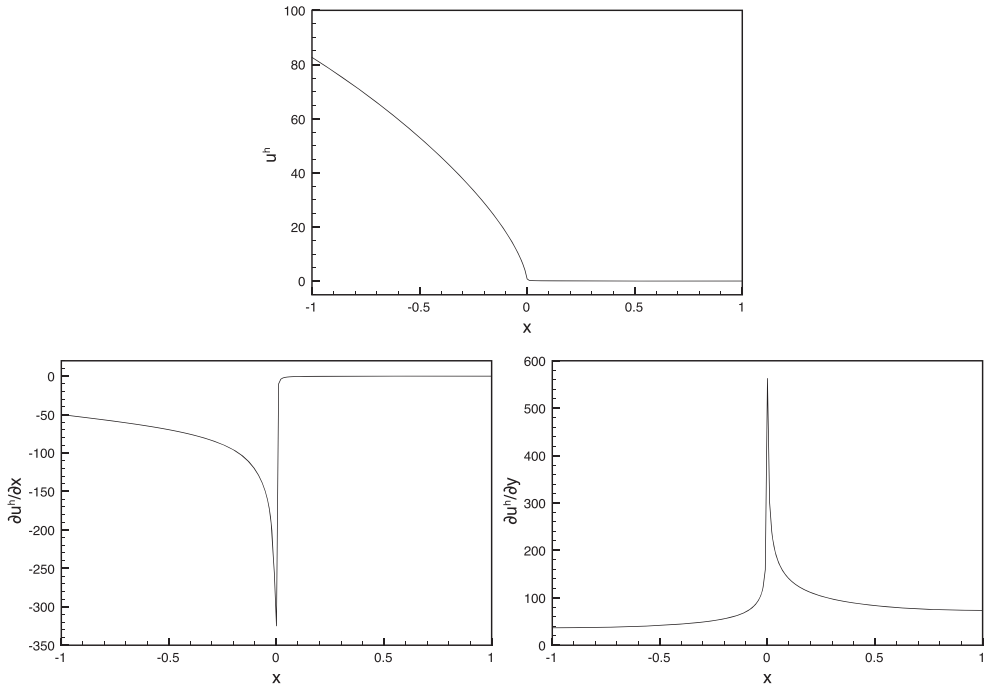

Figure 9. Fine-scale approximation along $y = 0.001$ of the solution of the L-shaped Poisson problem.

6.2.2. Discussion on error and stability in the reduced systems. The normalized errors in L_∞, L_2 and H^1 norms are shown in Figures 11–13, respectively, where the ISBFM-DR method provides better accuracy than the ISBFM-UR method. Even in the case where the reduced DOF is 80% of the full DOF, the error of the reduced solution from ISBFM-UR is still of the order $O(10^{-1})$. On the other hand, the solution of ISBFM-DR is much more accurate, where even just using $k \,/\, N = 5\%$ of the full DOF, the normalized error is of the order $O(10^{-2})$ when one and two non-smooth basis functions are used ($\hat{N} = 1$ and 2) and $O(10^{-3})$ when five non-smooth basis functions are used ($\hat{N} = 5$). This property in ISBFM-DR can be understood from the fact that when more non-smooth basis functions are used, the need for the smooth part of the approximation to approximate the singularity is reduced and thus leads to a more effective reduced-order approximation. This is not the case for ISBFM-UR, where the uniform projection of both smooth and non-smooth parts of the approximation significantly reduces its ability to approximate the singularity behavior in the reduced-order space as evidenced in Figures 11–13.

The error bounds provided in (43) and (44) show that the errors in sup-norm are related to the right-hand-side vector of the reduced discrete system with dimension k according to Equations (29a) and (29b). The numerical results described earlier demonstrate that the error from ISBFM-DR is dominated by the smooth part of the solution while the error from ISBFM-UR is dominated by the non-smooth solution. Table V compares the error bounds of ISBFM-UR and ISBFM-DR for the case when $\bar{N} = 1825$ and $\hat{N} = 1$ based on the analytical derivation in (43) and (44), respectively. These analytically predicted error ratios of the two reduced-order approaches are in the order of $O(10^{-3})$, which agrees quite well with the numerically calculated error results shown in Figure 11.

We also make the following observation: the L_∞ error norm of the ISBFM-DR method is about $O(10^{-3})$ of that from the ISBFM-UR method, regardless of the reduced-order dimension k. This can be understood from (43) and (44) in conjunction with the following reasons: (i) the eigenvalues λ_{k+1} of $\boldsymbol{K}$ and $\bar{\mu}_{\bar{k}+1}$ of $\bar{\boldsymbol{K}}^c$, shown in Table V, are quite similar; (ii) the ratio $\sqrt{N \,/\, \bar{N}}$ has a marginal influence on the error ratio when a small number of non-smooth basis functions are used; and (iii) the most influential factors on the error are the norms of the right-hand-side vector of the reduced systems, in this case, $\|\boldsymbol{f}\|_\infty = 178.86$ and $\|\bar{\boldsymbol{f}}^c\|_\infty = 0.60$, which essentially dominate the error bounds.

DOI: 10.1002/nme

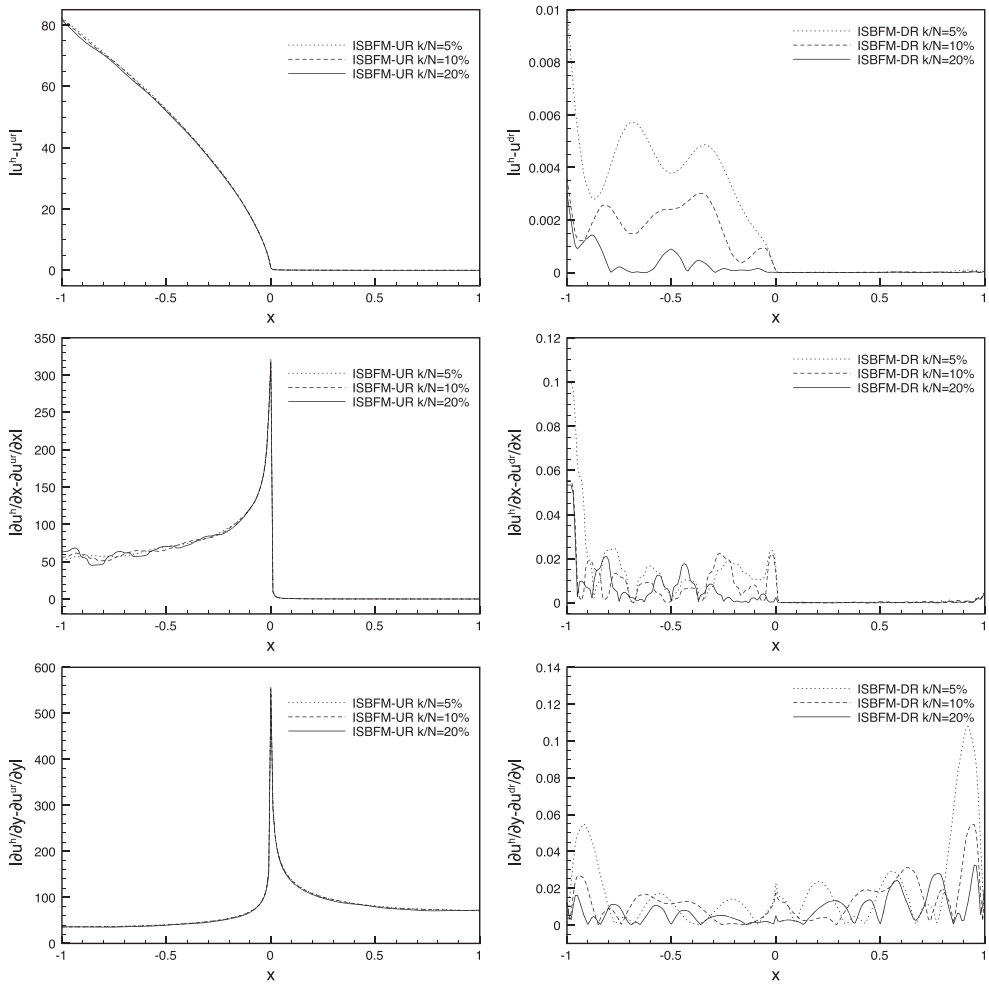

Figure 10. Absolute error distribution along $y = 0.001$ of the reduced solutions for the L-shaped Poisson problem with different percentages of k / N. DR, decomposed reduction; ISBFM, integrated singular basis function method; UR, uniform reduction.

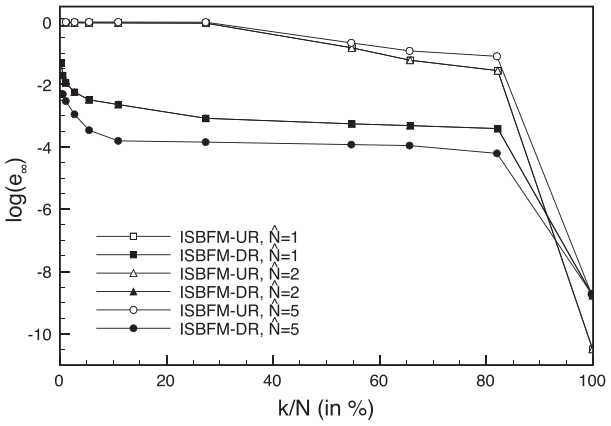

Figure 11. Normalized error in L_∞ norm for the L-shaped Poisson problem. DR, decomposed reduction; ISBFM, integrated singular basis function method; UR, uniform reduction.

DOI: 10.1002/nme

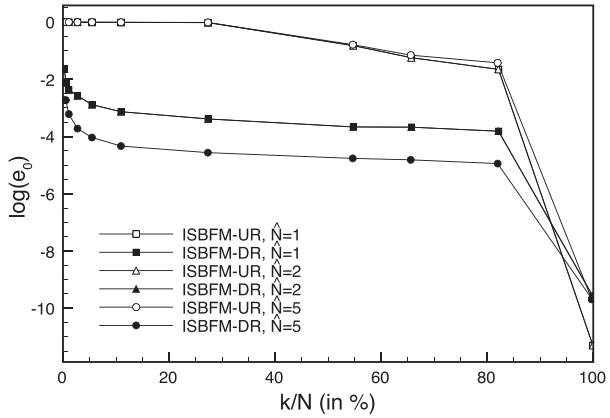

Figure 12. Normalized error in L_2 norm for the L-shaped Poisson problem. DR, decomposed reduction; ISBFM, integrated singular basis function method; UR, uniform reduction.

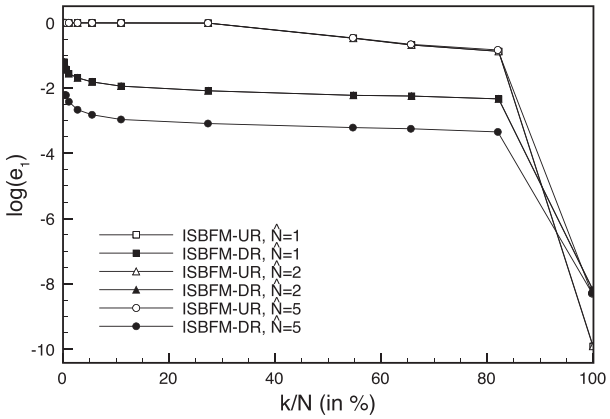

Figure 13. Normalized error in H^1 norm for the L-shaped Poisson problem. DR, decomposed reduction; ISBFM, integrated singular basis function method; UR, uniform reduction.

Table V. Analytically predicted error ratios between integrated singular basis function methods with decomposed reduction and uniform reduction for the L-shaped Poisson problem.

	k / N				
	0.5%	1%	5%	10%	20%
λ_{k+1}	$4.50\,10^{-2}$	$9.92\,10^{-2}$	$5.16\,10^{-1}$	$9.01\,10^{-1}$	$1.27\,10^{0}$
$\bar{\mu}_{\bar{k}+1}$	$3.91\,10^{-2}$	$9.89\,10^{-2}$	$5.01\,10^{-1}$	$8.98\,10^{-1}$	$1.27\,10^{0}$
$\frac{C_2\sqrt{N}\bar{\mu}_{\bar{k}+1}^{-1}\left\|\bar{f}^c\right\|_\infty}{C_1\sqrt{N}\lambda_{k+1}^{-1}\|f\|_\infty}$	$1.75\,10^{-3}$	$1.53\,10^{-3}$	$1.57\,10^{-3}$	$1.53\,10^{-3}$	$1.52\,10^{-3}$

Next, we perform a stability analysis of the reduced systems obtained from the ISBFM-DR and ISBFM-UR methods. The condition numbers of the reduced systems with various reduced dimensions are presented in Figure 14, and the ones of the fine-scale system are shown in Table VI. From the analytical predictions given in (49), the reduced systems from both MOR methods are better conditioned than the fine-scale system, which is in good agreement with the numerical results shown in Figure 14 and Table VI. It is worthy to note that the reduced system from ISBFM-UR has a slightly smaller condition number than the ones from ISBFM-DR shown in the numerical results

DOI: 10.1002/nme

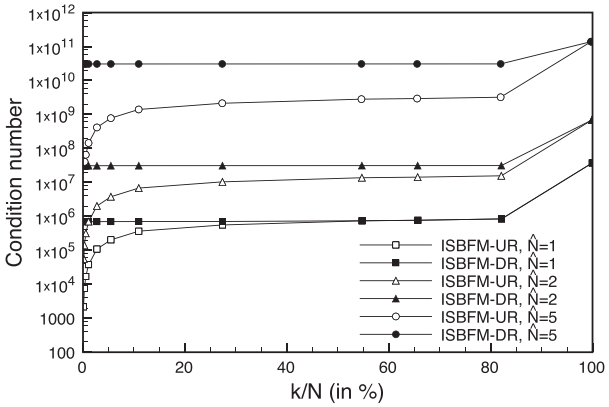

Figure 14. Condition number for the L-shaped Poisson problem. DR, decomposed reduction; ISBFM, integrated singular basis function method; UR, uniform reduction.

Table VI. Condition numbers of the full system for the L-shaped Poisson problem.

	$\bar{N} = 1825, \hat{N} = 1$	$\bar{N} = 1825, \hat{N} = 2$	$\bar{N} = 1825, \hat{N} = 5$
cond($\boldsymbol{K}$)	$3.73\,10^7$	$6.98\,10^8$	$1.43\,10^{11}$

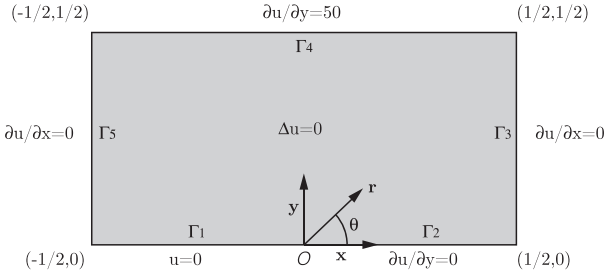

Figure 15. Model of cracked beam Poisson problem with prescribed traction.

in Figure 14. This was also predicted from our estimation of the condition numbers given in (53) in Section 5.2 when $(\hat{\mu}_{\hat{k}} + \varepsilon_N) \,/\, \lambda_1$ is sufficiently large.

6.3. Reduced-order modeling of a cracked beam Poisson problem

6.3.1. Problem statement and numerical results. The differential equation and boundary conditions of a cracked beam Poisson problem are given as follows:

$$\Delta u = 0 \quad \text{in} \quad \Omega$$
$$u|_{y=0,\,-1/2\leqslant x\leqslant 0} = 0$$
$$\left.\frac{\partial u}{\partial y}\right|_{y=0,\,0\leqslant x\leqslant 1/2} = 0, \quad \left.\frac{\partial u}{\partial x}\right|_{x=-1/2,\,0\leqslant y\leqslant 1/2} = 0, \quad \left.\frac{\partial u}{\partial y}\right|_{y=1/2,\,-1/2\leqslant x\leqslant 1/2} = 50, \quad \left.\frac{\partial u}{\partial x}\right|_{x=1/2,\,0\leqslant y\leqslant 1/2} = 0 \tag{60}$$

where $\Omega = (-1/2, 1/2) \times (0, 1/2)$. This cracked beam Poisson problem, described in Figure 15, possesses a stronger singularity than in the previous L-shaped Poisson problem.

The harmonic non-smooth basis functions F_m used in this problem are the same as in Equation (55) in the cracked beam Poisson problem of Section 6.1. In this model problem, the fine-scale solution is obtained from a 48×24 uniform nodal distribution ($\bar{N} = 1152$) with one

DOI: 10.1002/nme

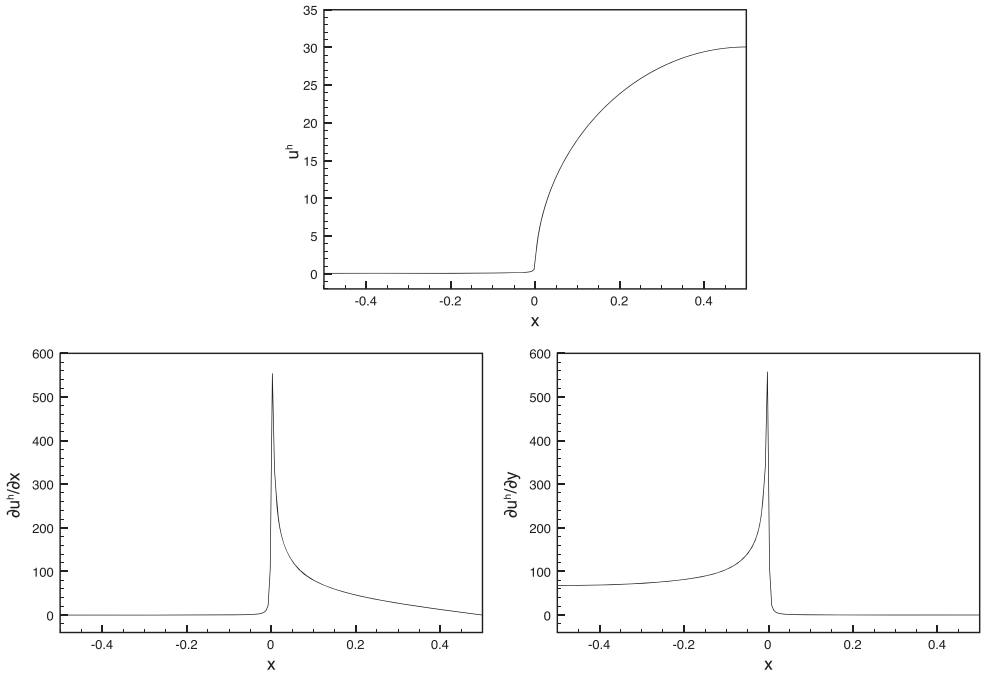

Figure 16. Fine-scale approximation along $y = 0.001$ of the solution of the cracked beam Poisson problem.

non-smooth basis function ($\hat{N} = 1$).

The solution approximation of the full model and its approximate derivatives are shown along $y = 0.001$ near the singularity point in Figure 16. Figure 17 presents a comparison of the absolute error distributions of reduced solutions from ISBFM-UR and ISBFM-DR for different percentages of reduction $k / N = 5\%$, 10%, and 20%, along $y = 0.001$. Compared with the ISBFM-UR approach, ISBFM-DR has a much smaller absolute error for all reduced dimension k. For low reduced dimension $k / N = 5\%$, the reduced solution from ISBFM-UR poorly approximates the fine-scale solution, although with improvement when $k / N = 10\%$. Note that in the L-shaped case, the error of the ISBFM-UR solution remains large unless a much larger reduced system is used.

6.3.2. Discussion on error and stability in the reduced system. From Figures 18–20, we can confirm that ISBFM-DR provides better accuracy in L_∞, L_2, and H^1 norm, especially in the cases where the dimension of the fine-scale system is greatly reduced. In this test, the reduced solution from ISBFM-UR approaches the full model with error in the order of $O(10^{-2})$ when the reduced dimension k is greater than 20% of the full dimension N. However, for k / N less than 10%, the solution from ISBFM-UR still produces significant errors. On the other hand, the accuracy of the reduced solution from ISBFM-DR is superior to that from ISBFM-UR in all ranges of order reduction.

The ratios of the analytical error bound of ISBFM-DR in (44) and the one of ISBFM-UR in (43) are given in Table VII for the case of $\bar{N} = 1152$ and $\hat{N} = 1$. Again, the analytical results show that the error in ISBFM-DR is smaller than that in ISBFM-UR, with the error ratio of the order $O(10^{-2})$, which is consistent with the numerical results shown in Figure 18. The error ratio between the two methods is mainly due to the norms $\|\boldsymbol{f}\|_\infty = 25.90$ and $\|\bar{\boldsymbol{f}}^c\|_\infty = 0.90$ following the analytical error bounds given in (43) and (44).

The condition numbers of the reduced system for this cracked beam Poisson problem can also be observed in Figure 21, and similar observations as that in the L-shaped Poisson problem are found. Compared with the condition numbers of the fine-scale system shown in Table VIII, we can see that the reduced systems are better conditioned, consistent with the analytical prediction in Section 5.

DOI: 10.1002/nme

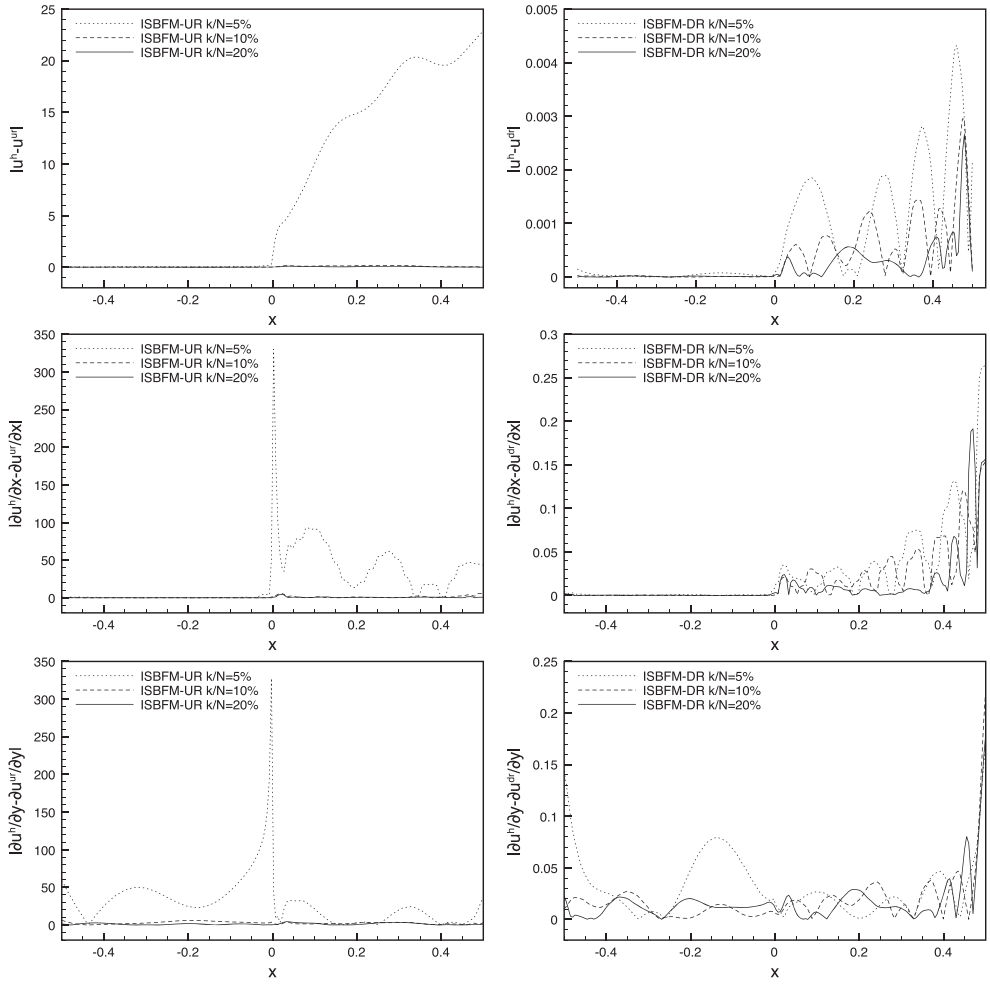

Figure 17. Absolute error distribution along $y = 0.001$ of the reduced approximations for the cracked beam Poisson problem with different percentages $k\ /\ N$. DR, decomposed reduction; ISBFM, integrated singular basis function method; UR, uniform reduction.

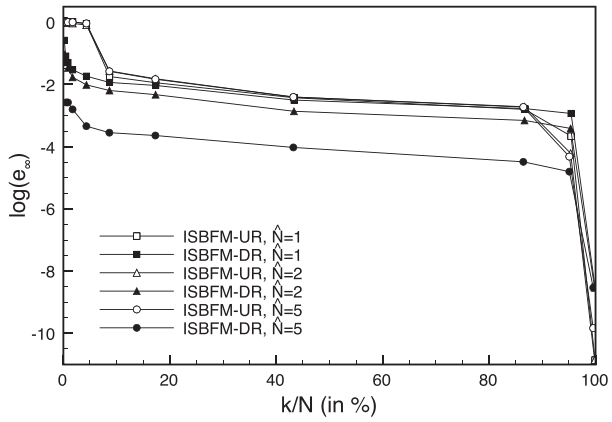

Figure 18. Normalized error in L_∞ norm for the cracked beam Poisson problem. DR, decomposed reduction; ISBFM, integrated singular basis function method; UR, uniform reduction.

DOI: 10.1002/nme

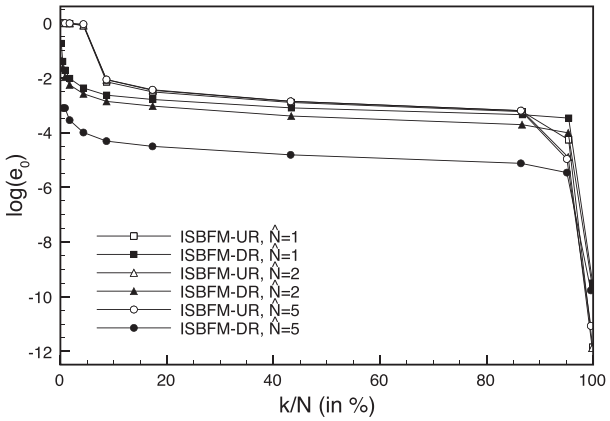

Figure 19. Normalized error in L_2 norm for the cracked beam Poisson problem. DR, decomposed reduction; ISBFM, integrated singular basis function method; UR, uniform reduction.

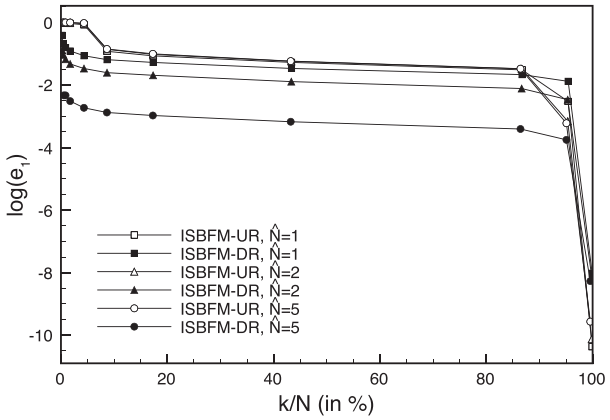

Figure 20. Normalized error in H^1 norm for the cracked beam Poisson problem. DR, decomposed reduction; ISBFM, integrated singular basis function method; UR, uniform reduction.

Table VII. Analytically predicted error ratios between integrated singular basis function methods with decomposed reduction and uniform reduction for the cracked beam Poisson problem.

	k / N				
	0.5%	1%	5%	10%	20%
λ_{k+1}	$4.46\,10^{-2}$	$1.05\,10^{-2}$	$4.85\,10^{-1}$	$8.65\,10^{-1}$	$1.22\,10^{0}$
$\bar{\mu}_{\bar{k}+1}$	$4.02\,10^{-2}$	$9.27\,10^{-2}$	$4.84\,10^{-1}$	$8.65\,10^{-1}$	$1.22\,10^{0}$
$\frac{C_2\sqrt{N}\bar{\mu}_{\bar{k}+1}^{-1}\left\|\bar{f}^c\right\|_\infty}{C_1\sqrt{N}\lambda_{k+1}^{-1}\|f\|_\infty}$	$2.23\,10^{-2}$	$2.28\,10^{-2}$	$2.02\,10^{-2}$	$2.02\,10^{-2}$	$2.02\,10^{-2}$

In this case, the condition numbers of both reduced models ISBFM-UR and ISBFM-DR are very similar, even though the reduced system from ISBFM-UR is slightly better conditioned than the one from ISBFM-DR.

DOI: 10.1002/nme

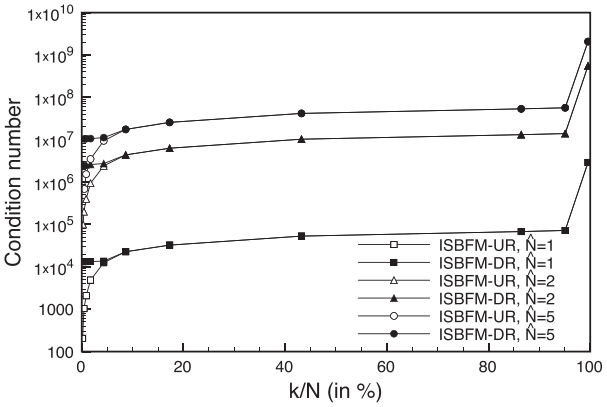

Figure 21. Condition number for the cracked beam Poisson problem.

Table VIII. Condition numbers of the full system for the cracked beam Poisson problem.

	$\bar{N} = 1152, \hat{N} = 1$	$\bar{N} = 1152, \hat{N} = 2$	$\bar{N} = 1152, \hat{N} = 5$
cond($\boldsymbol{K}$)	$2.94\,10^6$	$5.71\,10^8$	$2.33\,10^9$

7. CONCLUSIONS

Model order reduction techniques for enriched meshfree methods for problems with singularities and discontinuities have been presented in this paper. The characteristic of the model problem is that the accuracy of the reduced approximations is greatly affected by the singularity behavior of the full solution. In the proposed approach, the full approximation consisting of a smooth part from the RK approximation and a non-smooth part using asymptotic basis functions near the singularity point has been reduced by a standard MOR method and a new proposed MOR method. Analytical investigations on the errors, stability, and efficiency of the reduced systems from the proposed MOR methods have also been provided.

Under the framework of ISBFM, a modified Galerkin formulation is obtained in which the non-smooth basis functions appear only on integrals on the boundaries away from the singularity point. This approach avoids the need of higher-order integration in the domain and provides enhanced accuracy of the approximation, and it allows an effective DR method. Two ISBFM-based reduced-order projections have been developed for problems with singularities. The first MOR method is a UR method, termed ISBFM-UR, which projects all smooth and non-smooth DOFs to the reduced-order space. The second MOR method is a DR method, named ISBFM-DR, which intends to retain the singular behavior of the full solution in the reduced-order system. Because the number of non-smooth bases used is relatively small compared with the smooth DOF, the reduction of only the smooth part of the solution with Schur complement of the full system offers good performance. The analytical investigation of accuracy and stability of the reduced models has also been presented in this work.

The proposed MOR methods have been applied to Poisson singularity problems such as cracked beam problem and L-shaped problem. Error bounds of the proposed ISBFM-UR and ISBFM-DR methods have been derived and validated with numerical results. The numerical examples showed that keeping the non-smooth bases unprojected in the ISBFM-DR allows the reduced discrete system to properly capture the singularity behavior of the model problems. Numerical results showed that ISBFM-DR offers much better accuracy and faster convergence than ISBFM-UR with uniform projection for the entire approximation space. It has also been demonstrated numerically that the condition number of the reduced model from ISBFM-DR is only slightly increased compared with the one from ISBFM-UR method.

DOI: 10.1002/nme

REFERENCES

1. Antoulas AC, Sorensen DC. Approximation of large-scale dynamical systems: an overview. *Applied Mathematics and Computer Science* 2001; **11**(5):1093–1121.
2. Horn RA, Johnson CR. *Matrix Analysis*. Cambridge University Press: Cambridge, 2012.
3. Chatterjee A. An introduction to the proper orthogonal decomposition. *Current Science* 2000; **78**(7):808–817.
4. Kosambi DD. Statistics in function space. *Journal of the Indian Mathematical Society* 1943; **7**(1):76–88.
5. Loève M. Fonctions aléatoires de second ordre. *Comptes Rendus De L'Académie Des Sciences* 1945; **220**:380.
6. Everson R, Sirovich L. Karhunen-Loeve procedure for gappy data. *Journal of the Optical Society of America A* 1995; **12**(8):1657–1664.
7. Lumley JL. The structure of inhomogeneous turbulent flows, *Atmospheric Turbulence and Radio Wave Propagation*. Publishing House Nauka: Moscow, 1967.
8. Holmes P, Lumley JL, Berkooz G. *Turbulence, Coherent Structures, Dynamical Systems and Symmetry*. Cambridge University Press: Cambridge, 1998.
9. Lieu T, Farhat C, Lesoinne M. Reduced-order fluid/structure modeling of a complete aircraft configuration. *Computer Methods in Applied Mechanics and Engineering* 2006; **195**(41):5730–5742.
10. Ansallem D, Farhat C. Interpolation method for adapting reduced-order models and application to aeroelasticity. *AIAA Journal* 2008; **46**(7):1803–1813.
11. Hung ES, Senturia SD. Generating efficient dynamical models for microelectromechanical systems from a few finite-element simulation runs. *Journal of Microelectromechanical Systems* 1999; **8**(3):280–289.
12. Carlberg K, Farhat C. A low-cost, goal-oriented 'compact proper orthogonal decomposition' basis for model reduction of static systems. *International Journal for Numerical Methods in Engineering* 2011; **86**(3):381–402.
13. Boley DL. Krylov space methods on state-space control models. *Circuits, Systems and Signal Processing* 1994; **13**(6):733–758.
14. Cullum J, Zhang T. Two-sided Arnoldi and nonsymmetric Lanczos algorithms. *SIAM Journal on Matrix Analysis and Application* 2002; **24**(2):303–319.
15. Liu WK, Jun S, Zhang YF. Reproducing kernel particle methods. *International Journal for Numerical Methods in Fluids* 1995; **20**(8-9):1081–1106.
16. Chen JS, Pan C, Wu CT, Liu WK. Reproducing kernel particle methods for large deformation analysis of nonlinear structures. *Computer Methods in Applied Mechanics and Engineering* 1996; **139**(1):195–227.
17. Krysl P, Belytschko T. Element-free Galerkin: convergence of the continuous and discontinuous shape functions. *Computer Methods in Applied Mechanics and Engineering* 1997; **148**(3):257–277.
18. Li ZC, Mathon R, Sermer P. Boundary methods for solving elliptic problems with singularities and interfaces. *SIAM Journal on Numerical Analysis* 1987; **24**(3):487–498.
19. Li ZC, Lu TT. Singularities and treatments of elliptic boundary value problems. *Mathematical and Computer Modelling* 2000; **31**(8):97–145.
20. Fries TP, Belytschko T. The extended/generalized finite element method: an overview of the method and its applications. *International Journal for Numerical Methods in Engineering* 2010; **84**(3):253–304.
21. Moes N, Dolbow J, Belytschko T. A finite element method for crack growth without remeshing. *International Journal for Numerical Methods in Engineering* 1999; **46**:131–150.
22. Belytschko T, Black T. Elastic crack growth in finite elements with minimal remeshing. *International Journal for Numerical Methods in Engineering* 1999; **45**(5):601–620.
23. Fries TP. A corrected XFEM approximation without problems in blending elements. *International Journal for Numerical Methods in Engineering* 2008; **75**(5):503–532.
24. Fleming M, Chu YA, Moran B, Belytschko T, Lu YY, Gu L. Enriched element-free Galerkin methods for crack tip fields. *International Journal for Numerical Methods in Engineering* 1997; **40**(8):1483–1504.
25. Belytschko T, Lu YY, Gu L. Crack propagation by element-free Galerkin methods. *Engineering Fracture Mechanics* 1995; **51**(2):295–315.
26. Belytschko T, Fleming M. Smoothing, enrichment and contact in the element-free Galerkin method. *Computers & Structures* 1999; **71**(2):173–195.
27. Li ZC, Lu TT, Hu HY, Cheng AHD. Particular solutions of Laplace's equations on polygons and new models involving mild singularities. *Engineering Analysis with Boundary Elements* 2005; **29**(1):59–75.
28. Georgiou GC, Olson L, Smyrlis YS. A singular function boundary integral method for the Laplace equation. *Communications in Numerical Methods in Engineering* 1996; **12**(2):127–134.
29. Liao B-S, Bai Z, Gao W. The important modes of subsystems: a moment-matching approach. *International Journal for Numerical Methods in Engineering* 2007; **70**(13):1581–1597.
30. Reis T, Stykel T. A survey on model reduction of coupled systems. In *Model Order Reduction: Theory, Research Aspects and Applications*. Springer: Berlin, 2008; 133–155.
31. Vandendorpe A, Van Dooren P. Model reduction of interconnected systems. In *Model Order Reduction: Theory, Research Aspects and Applications*. Springer: Berlin, 2008; 305–321.
32. Lu TT, Hu HY, Li ZC. Highly accurate solutions of Motz's and the cracked beam problems. *Engineering Analysis with Boundary Elements* 2004; **28**(11):1387–1403.
33. Igarashi H, Honma T. A boundary element method for potential fields with corner singularities. *Applied Mathematical Modelling* 1996; **20**(11):847–852.
34. Li ZC, Lu TT, Hu HY, Cheng AHD. *Trefftz and Collocation Methods*. WIT Press: Southampton, 2008.

DOI: 10.1002/nme

35. Georgiou GC, Boudouvis A, Poullikkas A. Comparison of two methods for the computation of singular solutions in elliptic problems. *Journal of Computational and Applied Mathematics* 1997; **79**(2):277–290.
36. Olson LG, Georgiou GC, Schultz WW. An efficient finite element method for treating singularities in Laplace's equation. *Journal of Computational Physics* 1991; **96**(2):391–410.
37. Elliotis M, Georgiou G, Xenophontos C. Solving Laplacian problems with boundary singularities: a comparison of a singular function boundary integral method with the p/hp version of the finite element method. *Applied Mathematics and Computation* 2005; **169**(1):485–499.
38. Nitsche J. Über ein Variationsprinzip zur Lösung von Dirichlet-Problemen bei Verwendung von Teilräumen, die keinen Randbedingungen unterworfen sind. *Abhandlungen aus dem Matematischen Seminar der Universität Hamburg* 1971; **36**:9–15.
39. Fernández-Méndez S, Huerta A. Imposing essential boundary conditions in meshfree methods. *Computer Methods in Applied Mechanics and Engineering* 2004; **193**(12):1257–1275.
40. Chen JS, Wang HP. New boundary condition treatments in meshfree computation of contact problems. *Computer Methods in Applied Mechanics and Engineering* 2000; **187**(3):441–468.
41. Chen JS, Han W, You Y, Meng X. A reproducing kernel method with nodal interpolation property. *International Journal for Numerical Methods in Engineering* 2003; **56**(7):935–960.
42. Bergamaschi L, Putti M. Numerical comparison of iterative eigensolvers for large sparse symmetric positive definite matrices. *Computer Methods in Applied Mechanics and Engineering* 2002; **191**(45):5233–5247.
43. Lehoucq RB, Sorensen DC. Deflation techniques for an implicit restarted Arnoldi iteration. *SIAM Journal on Matrix Analysis and Applications* 1996; **17**(4):789–821.
44. Bai Z. *Templates for Solution of Algebraic Eigenvalue Problems: A Practical Guide*. SIAM: Philadelphia, 2000.
45. Hu HY, Lai CK, Chen JS. A study on convergence and complexity of reproducing kernel collocation method. *Interaction and Multiscale Mechanics* 2009; **2**:295–319.
46. Press WH, Flannery BP, Teukolsky SA, Vetterling WT. *Numerical Recipes, The Art of Scientific Computing*. Cambridge University Press: Cambridge, 1986.
47. Golub GH, van Van Loan CF. *Matrix Computations* (3rd edn). The Johns Hopkins University Press: Baltimore and London, 1996.

DOI: 10.1002/nme